

**THE IMPACT OF SMALL-SCALE LANGMUIR CIRCULATIONS
ON AIR-WATER INTERFACE AND SURFACE COOL SKIN**

by
Yi Ma

A thesis submitted to the Faculty of the University of Delaware in partial fulfillment of the requirements for the degree of Master of Science in Marine Studies

2016 Summer

© 2016 Yi Ma
All Rights Reserved

ProQuest Number: 10192162

All rights reserved

INFORMATION TO ALL USERS

The quality of this reproduction is dependent upon the quality of the copy submitted.

In the unlikely event that the author did not send a complete manuscript and there are missing pages, these will be noted. Also, if material had to be removed, a note will indicate the deletion.



ProQuest 10192162

Published by ProQuest LLC (2016). Copyright of the Dissertation is held by the Author.

All rights reserved.

This work is protected against unauthorized copying under Title 17, United States Code
Microform Edition © ProQuest LLC.

ProQuest LLC.
789 East Eisenhower Parkway
P.O. Box 1346
Ann Arbor, MI 48106 - 1346

THE IMPACT OF SMALL-SCALE LANGMUIR CIRCULATIONS
ON AIR-WATER INTERFACE AND SURFACE COOL SKIN

by
Yi Ma

Approved: _____
Fabrice Veron, Ph.D.
Professor in charge of thesis on behalf of the Advisory Committee

Approved: _____
Mark A. Moline, Ph.D.
Director of the School of Marine Science and Policy

Approved: _____
Mohsen Badiy, Ph.D.
Acting Dean of the College of Earth, Ocean, and Environment

Approved: _____
Ann L. Ardis, Ph.D.
Senior Vice Provost for Graduate and Professional Education

ACKNOWLEDGMENTS

I would like to thank my advisor Fabrice Veron, for guiding me academically, he gave me enough freedom and patience. He motivated my passion for research. I enjoyed my work.

Next, I would like to thank for the people in P.O.S.E. program and Robinson 210, for their help as friends and as scientists.

The support that I get from my family and friends, I really appreciate it.

TABLE OF CONTENTS

LIST OF TABLES	vii
LIST OF FIGURES	ix
ABSTRACT	xiii
 Chapter	
1 INTRODUCTION	1
1.1 Short introduction to the phenomena	1
1.2 Theory	4
1.3 Small scale Langmuir Circulations	7
2 EXPERIMENTAL SETUP	11
2.1 Experiment Techniques	11
2.2 Methods	15
2.2.1 Particle Image Velocimetry	16
2.2.2 Thermal Marking Velocimetry	18
2.2.3 Controlled Flux Techniques	20
3 RESULTS	23
3.1 Waves and Winds	24
3.1.1 Winds and wave height	24
3.1.2 Wave spectrum	27
3.1.3 Initial scales of winds and waves	28
3.2 Surface Thermography—Passive Infrared Imaging	28
3.2.1 Flow Visualization	30

3.2.2	Statistics of the Flow	35
3.2.2.1	Temperature Standard Deviation	35
3.2.2.2	Time Series of Mean Temperature	39
3.3	Surface Thermography—Active Infrared Imaging	40
3.3.1	Velocity-Momentum Boundary Layer	41
3.3.2	Thermal Boundary Layer	43
3.4	Subsurface Statistics Measurements	45
3.4.1	Cross-wind Direction	45
3.4.1.1	LC's evolution	45
3.4.1.2	Velocity in horizontal and vertical direction	47
3.4.2	Along-wind direction	50
3.4.2.1	LC's evolution and horizontal velocity	50
3.4.2.2	Enstrophy	54
3.4.2.3	Velocity	56
4	DISCUSSION	58
4.1	Inception of Surface Waves and Langmuir Circulations	58
4.2	Comparison between PIV and Infrared Data	61
4.2.1	Velocity	61
4.2.2	Other parameters	62
4.3	Comparison of the momentum and heat flux.	62
4.4	Heat and gas flux	65
4.5	Temperature difference	67
4.6	Scaling the instabilities	67
4.6.1	Non-dimensional parameters	67
4.6.2	Langmuir number	71
	BIBLIOGRAPHY	73

Appendix

A TEMPERATURE RATIO 76

LIST OF TABLES

2.1	A summary of all imagery properties in transverse direction.	14
2.2	A summary of all imagery properties in longitudinal direction.	14
2.3	Summary of the wind data for the four cases.	15
3.1	Summary of wind and wave statistical parameters of the four cases	29
3.2	Summary of the time and length scale of the inception of the LC.	35
3.3	Summary of standard deviation of the surface temperature measured by infrared camera.	37
3.4	Summary of Surface Velocity of the Four Cases.	43
3.5	Measured surface wave parameters at the inception of the LC of the four cases.	43
3.6	Summary of Decay Rate.	45
3.7	Summary of surface velocity by cross correlation method of the four cases	57
4.1	Summary of heat and gas flux of the four cases.	68
4.2	Summary of temperature difference, ΔT between maximum temperature and the mean temperature of the four cases at the LC inception time.	69
4.3	Summary of Reynolds number and Raleigh number of the four cases.	71
4.4	Summary of Langmuir number and the turbulent Langmuir number for the four cases.	72

A.1	Summary of ratio of the maximum temperature to mean temperature of the infrared temperature data.	78
-----	---	----

LIST OF FIGURES

1.1	Windrows comprised mainly of foam from breaking waves in the lake, Loch Ness. The surface convergence regions were marked as the Langmuir Circulation (Thorpe, 2004).	2
1.2	subsurface bands of toxix algae in German Bight of the North Sea in August, 1988. The bands were a few meters apart.(Thorpe, 2004) .	3
1.3	Sketch showing the pattern of mean flow in idealized Langmuir Circulation in field (Thorpe, 2004).	5
1.4	Sketch illustrating the CLII theory by Leibovich (1983)	6
1.5	A conceptual sketch of the molecular layers for momentum, temperature and gas concentration (CO ₂)	7
1.6	Small-scale Langmuir Circulations cut of current lab work at time 29.78 s after the wind started to blow the quiescent water. z is the depth and x is the across-wind direction water width.	8
2.1	Experiments setup in different direction, the panel on the left showing the along-wind direction while the panel on the right showing the cross-wind direction	11
2.2	A closer look at the PIV cameras layout	13
2.3	Four cases with different wind speed and acceleration.	15
2.4	Experimental arrangement for particle image velocimetry (Raffel et al., 2013).	16
2.5	Conceptual arrangement of frame-to-frame image sampling associated with double frame/single exposure Particle Image Velocimetry (Raffel et al., 2013).	18

2.6	An example of a surface temperature image when active heat dots are visible using TMV, the wind is going from left to right in these infrared images.	19
3.1	Time series of the wind speed for the four cases. Also shown are the four recording time for the Infrared Cameras and PIV cameras. The wind speed before it reaches to the final highest speed matches the equation 3.1 for each case.	24
3.2	Wave height rms for the four cases.	25
3.3	Time series of the wind speed for the four cases. Black dots indicate the evolution time of LC for each case	26
3.4	(a) is the wave spectrogram of surface displacement recorded by the wire wave gauge for a final wind speed of $10.2m/s$ for Case 1. (b) is the time evolution of the peak frequency. (c) is the the peak energy density.	27
3.5	Evolution of the temperature surface flow of the Case 1 — the four stages mentioned in the section. The four figures show the time evolution of the surface flow of the four stages. x is the direction of the flow while y is the cross-wind direction. The temperature is given by the colorbar.	31
3.6	Infrared images showing the development and evolution of LC imaged by the surface temperature as a function of time for Case 1. Images sizes are $24.7\text{ cm} \times 24.7\text{ cm}$. The wind is blowing from left to right. Time shown since the inception of the wind are from 28.5-31s from the start of the wind, in 0.5s increments. The temperature is given by the colorbar.	33
3.7	The surface temperature field showing the LC for the four cases. . .	34
3.8	Normalized standard deviation of the highpass temperature, α , for the four cases. The red dots in the figure are the LC inception time.	35
3.9	Time series of a cross-wind cut of the highpass temperature. The band at top and bottom of the figure is noise introduced by the camera lens.	38

3.10	The time series of the mean temperature in the cross-wind cut with a 8-second time between before LC inception and turbulence of the four cases.	39
3.11	Three dimensional representation of the surface temperature. The horizontal images are the figure 3.6. The vertical image shows a highpassed temperature cross-wind cut though the surface images with time as figure 3.12. The colorbar in the left-hand side is the colorbar for the vertical image while the colorbar in the right-hand side is the colorbar for the horizontal images.	40
3.12	Heat spots example of a surface temperature image where active heat dots are visible.	41
3.13	The surface velocity for the four cases. Different colors indicate different cases. Only 30 seconds of data around the inception of the LC are shown here. The red dots in the figure are the LC inception time.	42
3.14	Decay rate of the heat markers for the four cases.	44
3.15	The inception and evolution of LC in cross-wind direction for Case 1, the gray scales in the figure is fluorescent dye in the water, which has no influence on the dynamics.	46
3.16	The inception and evolution of LC in cross-wind direction of the vertical velocity of Case 1.	48
3.17	The inception and evolution of LC in cross-wind direction of the horizontal velocity of Case 1.	49
3.18	The inception and evolution of LC in along-wind direction imaged with LIF of Case 1.	51
3.19	The inception and evolution of LC in along-wind direction of the vertical velocity of Case 1. The colorbar indicates the vertical velocity.	53
3.20	The vorticity square profiles and the upper layer of the averaged kinetic energy of Case 1.	54
3.21	The vorticity square profiles and the upper layer of the averaged vorticity square of Case 2, 3, and 4.	55

3.22	Measured surface velocity by cross correlation method of the PIV data along-wind direction.	56
4.1	Parameters comparison showing the wind speed, the wave height rms, and the wave peak frequency.	59
4.2	Peak frequency for the four cases.	60
4.3	Comparison of the velocity by PIV method and TMV method. . .	61
4.4	Comparison of velocity, vorticity and velocity by PIV method for the four cases.	62
4.5	Parameters comparison of the surface velocity, vorticity square (entrosphy), surface temperature decay rate, and highpass temperature deviation by the infrared and PIV data and the TMV methods.	63
4.6	The comparison of the momentum data of the Case 1. Different colors means different stage of the flow.	64
4.7	The comparison of the thermal data of the Case 1. Different colors means different stage of the flow.	65
4.8	The heat transfer velocity of the four cases. The red dots marked in the figure are the LC inception time for each case.	66
4.9	The difference, ΔT between maximum temperature and the mean temperature of the four cases. Different color indicates different cases. The red dots are the LC inception time.	69
4.10	The temperature difference, ΔT between maximum temperature and the mean temperature of the four cases. The red dots in the figure are the LC inception time.	70
A.1	The maximum temperature, the mean temperature, and the ratio of maximum temperature to the mean temperature of four cases. The red dots in the figure are the LC inception time.	77
A.2	The ratio of maximum temperature to the mean temperature of the four cases. Different color indicates different cases. The red dots are the LC inception time.	79

ABSTRACT

Mixing and turbulence take a great role in air-sea interactions nowadays. When wind starts to blow over a quiescent air-sea interface, both currents and surface waves are initially generated. The interaction between the wind-driven waves and currents leads to the generation of Langmuir circulation (LC) consisting of counter rotating vortices aligned with the wind. Shortly thereafter, Langmuir turbulence (LT), that is multiple scales of LC, appear. In LT, length scales range from several centimeters when short capillary waves first appear up to tens of meters when the spectrum of waves broadens.

The main purpose of this thesis is to research how small-scale LC develops and evolves and its impact to mixing and turbulence, especially on the disruption of the near surface molecular layers of heat and momentum.

The results are from laboratory experiments performed at the air-sea interaction lab at University of Delaware in Lewes DE. In this experiment, we used surface infrared imagery and subsurface Particle Image Velocitmetry techniques. We saw that the evolution of from organized small scale LC to LT is very rapid leading to intense surface mixing whereby momentum initially transferred to the surface through viscosity efficiently mixes the near surface layers. Subsurface turbulence measurements are presented in the context of scalar (gas) flux through the air-water interface.

Chapter 1

INTRODUCTION

1.1 Short introduction to the phenomena

The atmosphere and the ocean are a coupled system. They constantly exchange mass, heat, momentum, and energy. The earth surface is covered with approximately 70% of water, thus, air-sea interactions play a vital role in marine environmental and atmospheric systems. All these interactions between the atmosphere and the ocean shape our weather and global climate change. For example, the energy from the wind blowing over the surface of the ocean produces waves and currents and small-scale near-surface turbulence which can potentially affect the surface heat fluxes ([Veron et al., 2011](#)).

Wave breaking and other wave-related phenomena play a highly vital role in air-sea interactions. They enhance air-sea fluxes of heat, mass, and momentum through the generation of turbulence and entrainment of air ([Melville, 1996](#)). Breaking, as a strongly nonlinear process, is playing a series of related roles in air-sea interaction. Breaking is the source of vorticity and turbulence, some of which is used for turbulent mixing and dissipating surface-wave energy. Finally, it enhances gas and heat transfer via surface turbulence and bubble.

From [Figure 1.1](#), at the surface of wind-driven oceans or lakes, one can often observe long streaks or windrows approximately aligned with the wind direction. Those signs are streaks of floating material or bubbles that collect on the water surface.

Those are meter-scale (large-scale) Langmuir circulations. In 1938, Irving Langmuir observed the phenomena and demonstrated that those streaks were associated with subsurface longitudinal counter-rotating vortices in a lake ([Langmuir, 1938](#)). This phenomenon now bears his name.



Figure 1.1: Windrows comprised mainly of foam from breaking waves in the lake, Loch Ness. The surface convergence regions were marked as the Langmuir Circulation (Thorpe, 2004).

Figure 1.2 shows the bands comprised of the toxic algae in the German Bight of the North Sea in August 1988, which indicates that the bands of the bubbles or buoyant algae may form the downwelling flow as well.

There are different scales of Langmuir Circulations. From what we usually see in the field, the windrows can be $2m$ to $300m$, while there is some small-scale LC with large-scale LC, the small-scale ones are usually smaller than $O(1)m$.

Langmuir (1938) stated:

“Quantitative measurements of the streak spacings are difficult because between the well defined streaks there are numerous smaller and less well-defined streaks. Just as large waves have smaller waves upon them, it appears that surfaces of large vortices contain smaller and shallower vortices.”

In this statement, the small-scale, transient, Langmuir circulations (which is usually under $O(1)m$) do exist. However, because of the technology limit, scientists usually observed large-scale Langmuir Circulations.

Since Langmuir's observation in 1938, numerous other observations using novel



Figure 1.2: subsurface bands of toxic algae in German Bight of the North Sea in August, 1988. The bands were a few meters apart. (Thorpe, 2004)

techniques have been made. [Weller et al. \(1985\)](#) and [Weller and Price \(1988\)](#) used several different instruments, such as vertical profilers, vector measuring current meters, and sonars deployed from (R/P FLIP) to observe LCs. They showed three-dimensional flow within the mixed layers and the existence of strong Langmuir cells. They observed the surface convergence lines extending up to 2 km in length, with cross-wind scales, ranging from 120 to 180 m.

[Smith \(1992\)](#) described acoustic Doppler velocity measurements off the California coast and showed the growth of Langmuir circulations. He also indicated that the ratio of spacing and depth of Langmuir circulation cells is accelerating as the LC develops.

LC now is regarded as a vital turbulent process in producing and maintaining the uniform surface mixed layer. It also plays a crucial role in driving dispersion and producing and maintaining the uniform surface mixed layer ([Thorpe, 2004](#)).

1.2 Theory

Figure 1.3 indicates the pattern of mean flow in idealized Langmuir Circulation. The windrows are along the same directions as the wind, and may be 2 m to 300 m apart. The cell of Langmuir Circulation is roughly square. In the field the flow is turbulent. Bands of bubbles or buoyant algae may form within the downwelling flow.

A number of mechanisms and ideas were proposed since Langmuir first reported his observations in 1938. However nowadays, it is accepted that oceanic scales Langmuir circulations result from the interaction of the Stokes drifts generated by the waves with the near surface shear currents. [Craik \(1977\)](#) and [Leibovich \(1977\)](#) first identified this mechanism and summarized it in what is now known as the Craik-Leibovich (CLII) framework.

In short, when the wind blows in a fixed direction over an unlimited horizontal extent and depth of water, the development of a surface wave field with unidirectional Stokes drift aligned with the wind.

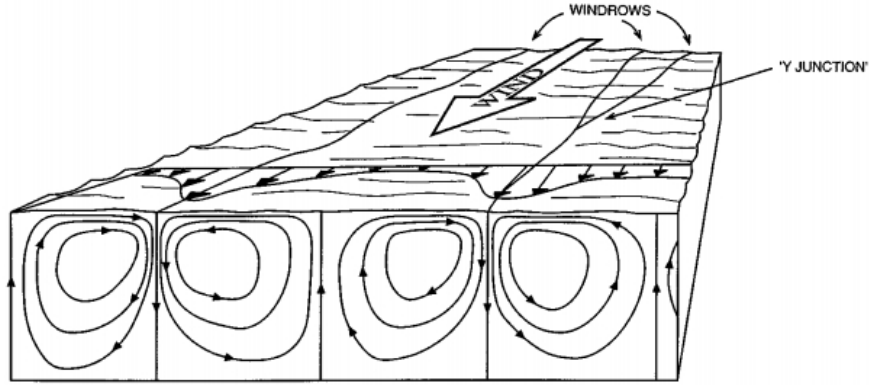


Figure 1.3: Sketch showing the pattern of mean flow in idealized Langmuir Circulation in field (Thorpe, 2004).

Under Boussinesq approximation and the assumption of constant eddy diffusivities of momentum (γ_T) and heat (α_T), Craik-Leibovich equations are

$$\frac{\partial \mathbf{u}}{\partial t} + \mathbf{u} \cdot \nabla \mathbf{u} = -\nabla \pi + u_s \times \nabla \times \mathbf{u} + \beta \mathbf{g} \theta + \gamma_T \nabla^2 \mathbf{u} \quad (1.1)$$

θ is the temperature perturbation, β is the coefficient of thermal expansion, \mathbf{u} is the mean velocity vector in the currents, π is modified pressure term. $\beta \mathbf{g} \theta$ is the buoyancy term and $\gamma_T \nabla^2 \mathbf{u}$ is the stress term.

Equation 1.1 only altered by the appearance of an apparent “vortex force”, that is

$$\mathbf{f} = u_s \times \omega \quad (1.2)$$

ω is the mean vorticity, so the second term in the right hand side of equation 1.1 is vortex force. u_s is along the wave direction (x direction) and is horizontal, but decays in depth. Physically, vertical gradient of Stokes drift tilts existing vertical vortex lines. So the streamwise vorticity is in vertical direction (z direction). Consequently, horizontal vortex force $\mathbf{f} = u_s \times \omega$ is in y direction, variations of the vortex force create a torque to overturn the water. And depending on the upward vertical direction and downward direction, there will be convergence zone and divergence zone. The white streaks which

Langmuir number is a non-unit number which can also be reviewed as an inverse Reynolds number (Leibovich, 1983). It expresses a balance between the rate of diffusion and the rate of production of streamwise vorticity from the vortex stretching caused by the Stokes drift.

1.3 Small scale Langmuir Circulations

In recent years, the global climate change and the growing pollution in atmosphere and oceans have drawn the attention to small-scale transfer processes at the air/water interface (Schimpf et al., 1999).

The air-sea heat fluxes are mainly through the molecular, diffusive sublayer at the ocean surface. Seeing figure 1.5 from left to right, the thickness of momentum viscous layer is on the order of 1-2 mm, that of the thermal boundary layer is on the order of 1 mm, while the thickness of the gas (concentration) diffusion layer is about one-fourth that of the cool skin layer (Doney, 1995). Here, U_s , T_s , and C_s are the velocity, temperature, and concentration at the surface.

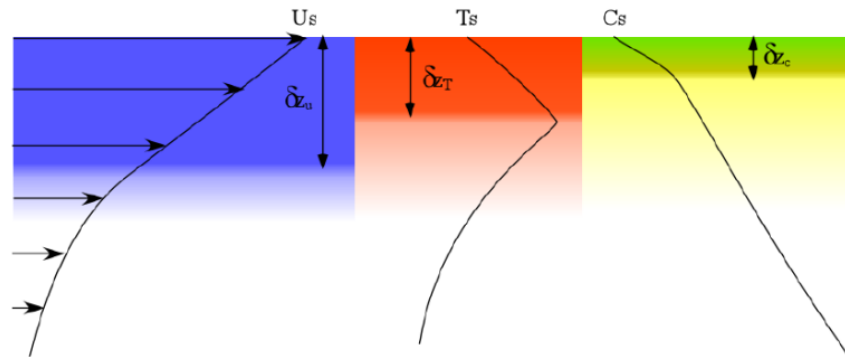


Figure 1.5: A conceptual sketch of the molecular layers for momentum, temperature and gas concentration (CO_2)

As shown in Figure 1.5, the gas concentration layer is embedded within the thermal boundary layer, the thermal and gas concentration sublayer is embedded within

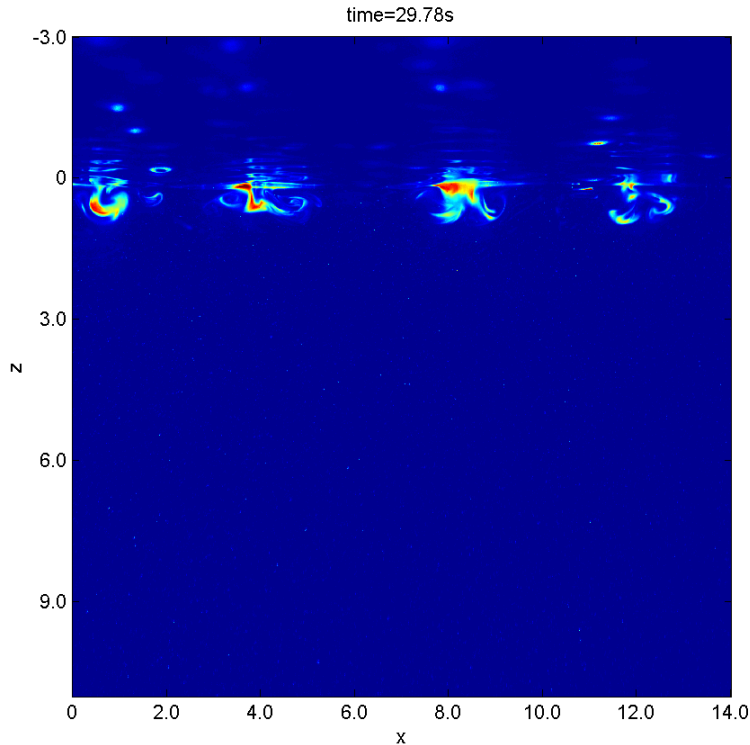


Figure 1.6: Small-scale Langmuir Circulations cut of current lab work at time 29.78 s after the wind started to blow the quiescent water. z is the depth and x is the across-wind direction water width.

the viscous sublayer in the uppermost mixed layers of the ocean. Consequently, the air-sea heat exchange rate is dependent on the surface kinematics and dynamics.

Small-scale Langmuir circulations are expected to influence the structure of the near-surface kinematics (and the near surface molecular layers), thus potentially influencing the ocean-atmosphere fluxes of heat and gas.

Indeed, [Melville et al. \(1998\)](#) and [Veron et al. \(1999\)](#), small-scale LC led to a rapid mixing of the surface layer. As a result, [Veron and Melville \(2001\)](#) showed that LCs provide a rapid and efficient way of disrupting the surface thermal boundary layer.

Small-scale LC is mainly understood as centimeter-scale ($O(1 - 10)$ cm) Langmuir circulations. They are difficult to observe in the field and that's the reason why small-scale LC and the associated mixing and turbulence are still poorly understood ([Veron et al., 2008](#)).

Figure 1.6 is the current laboratory work of small-scale LC in Air-sea Interaction Laboratory in Lewes in University of Delaware. This is an across-wind direction sub-surface Particle Image Velocimetry (PIV) image. The z axis is the depth of the water. 0 means the water surface. The optical LC was the dye in the surface of the water, we will talk about the PIV method in Chapter 2.

However, small-scale LC has a tight relation with the rapid development of the surface gravity-capillary waves; the small-scale LC supports the transition from laminar to turbulent surface flow as well as being quick to appear with the gustiness in the wind field. Therefore, those small-scale LCs can provide intense and prompt turbulent bursts at the surface which may dominate the average surface renewal processes. Besides, the intermittent nature of small-scale Langmuir circulations has a key impact on the sublayers of the ocean in long-term behavior, especially under low wind speed circumstances (Veron et al., 2008).

Overall, very few observations and simulation of small-scale LC exists. Kenney (1993), observed small-scale LC as coherent bands of algae in a surface shear layer.

In 1998, Melville et al. (1998) and co-workers set up laboratory experiments on the generation and evolution of small scale Langmuir circulations. The Langmuir circulations appear as an instability in the wind-driven surface shear layer driven by the accelerating wind. They also found that the Langmuir circulations led to a quick and fast turbulent transition and led to significant vertical mixing in the surface layer. In the experiment, they observed that the size of the LC scales with the shear layer depth.

In 2001, Veron and Melville (2001) did quantitative laboratory and field measurements on the stability of wind-driven water surfaces. They showed that the instability of the surface shear flow to LCs, and the following rapid transition to turbulence are considered to be a vital and important transition to the transfer of momentum, heat and gas across water surface at low wind speeds. The inception of small-scale Langmuir circulations leads to 70% increase in gas transfer.

In 2008, Veron et al. (2008) did field experiments conducted from *R/PFLIP*

moored nearly 150 miles off the coast of southern California. They observed breaking waves generate turbulence along with small-scale Langmuir circulations and coherent structure using infrared cameras and PIV techniques, and they presented evidence of the existence of small-scale (submeter-scale) Langmuir circulations.

Their observations show the existence of small-scale, transient Langmuir circulations in field and laboratory as well. The aim of this project is to understand the impact of small-scale LC on transfer heat and gas transfer at an air-water interface.

Chapter 2

EXPERIMENTAL SETUP

The aim of this thesis is to perform laboratory experiments on the generation of small scale LC and subsequent Langmuir turbulence.

2.1 Experiment Techniques

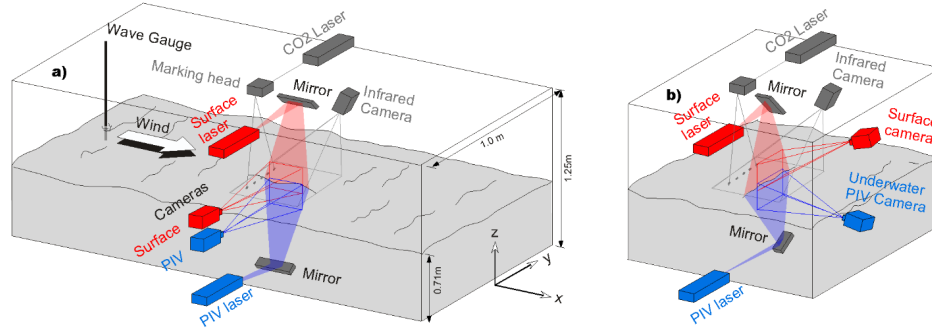


Figure 2.1: Experiments setup in different direction, the panel on the left showing the along-wind direction while the panel on the right showing the cross-wind direction

The experiments were performed in the large wind-wave-current facility at the air-sea interaction laboratory of University of Delaware on the Lewes campus. The main facility of the air-sea interaction laboratory is a 42-meter long, 1-meter wide and 1.30-meter high wind-wave-current tank. We used the tank with the recirculating wind tunnel.

There are roughly 10 to 15 experiment techniques were used in the laboratory work. From Figure 2.1, we used four wave gauges to measure the wave height of the waves.

There are 2 lasers and 2 cameras. One laser is used for PIV and one camera is used for PIV. The other laser/camera pair is used for the LIF to detect the position of the surface.

In the water, we had some particles, which were very small and had no influence on the experiments. We used $10\mu m$ particles coated with 22% silver (density = $1.4g/cm^3$) to have a better visibility on PIV images. In addition, rhodamine 6g was added to the water and used to detect the surface for the PIV computation. Dye was also put into the surface of the water, and was used to see how the LC evolved.

Besides the PIV cameras, an infrared camera was also used in these experiments. It was at the top of the tank, looking at the water surface, and measuring the surface temperature. The infrared imaging was used in two different modes: active and passive IR measurements were made. Passive IR simply consists of detecting the surface temperature with the cameras while active IR makes use of a CO_2 laser to actively lay down heat markers. The heat markers will be used as Lagrangian surface markers and their rate of heat decay will also serve as a proxy for interfacial heat flux.

The right panel of Figure 2.1 shows the instrumentation setup for measurements in the crosswind plane.

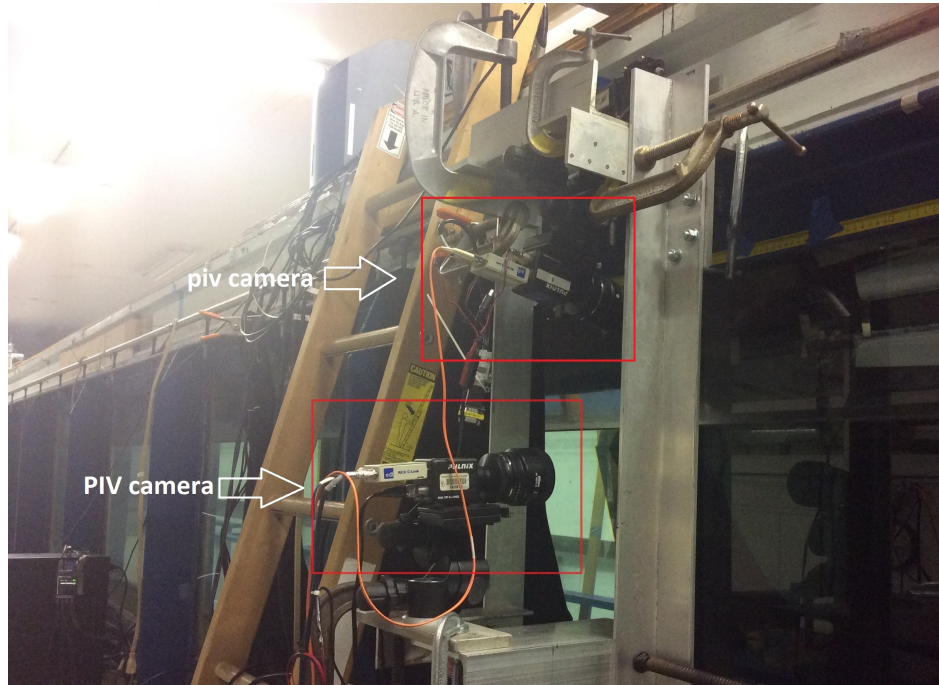


Figure 2.2: A closer look at the PIV cameras layout

In all cases, PIV images were acquired at 14.4 Hz giving 7.2 velocity maps per second. Heat markers were laid down at 0.48 Hz. The IR camera frame rate was 43.2 Hz. All cameras and lasers were synchronized. Finally, 4 different wind speed and accelerations were studied. For each experimental setup, several repeats for performed in order to collect relevant statistics.

We used one PIV camera, one LIF camera and one infrared camera to detect the water surface as well as the water under the surface.

The Table 2.1 and Table 2.2 are the tables of two sets experiments, the size of the camera lens, and its area size of the water.

Camera	Lens(mm)	Area Size (cm × cm)
Underwater PIV camera	85.00	13.88 × 13.88
PIV surface camera	50.00	23.65 × 23.65
IR camera	50.00	24.57 × 24.57

Table 2.1: A summary of all imagery properties in transverse direction.

Methods	Lens(mm)	Size (cm × cm)
Underwater PIV camera	85.00	11.59 × 11.59
PIV surface cameras	50.00	20.00 × 20.00
IR cameras	50.00	24.57 × 24.57

Table 2.2: A summary of all imagery properties in longitudinal direction.

In these four different cases, we have different final wind speed as well as different wind acceleration.

See the Table 2.3, there are four cases with different wind acceleration and final wind speed in each set. Each case has been repeated three times. Figure 2.3 indicates the difference of four cases by visualization. The four cases all started at $t = 0s$ as when the wind started. However, in order to be able to capture the inception of the LC, the beginning of the recording time was different.

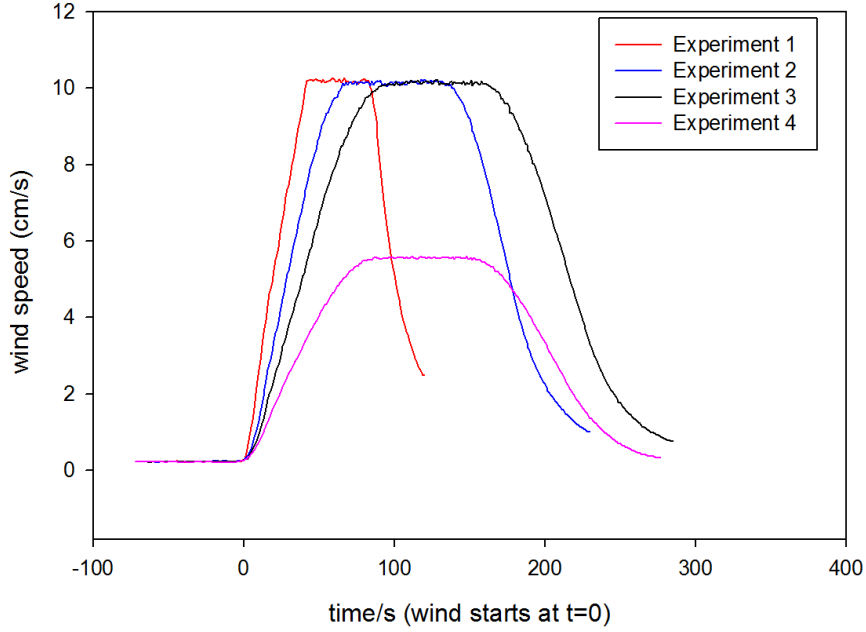


Figure 2.3: Four cases with different wind speed and acceleration.

Cases	Recording time(s)	Wind Acceleration(m/s^2)	Final Wind Speed(m/s)
1	12.00	0.2453	10.20
2	18.00	0.1917	10.15
3	28.00	0.1427	10.13
4	43.00	0.0792	5.56

Table 2.3: Summary of the wind data for the four cases.

2.2 Methods

In this project, we collected the main data sets using three techniques, high resolution digital imaging techniques PIV (Particle Image Velocimetry), infrared imaging techniques TMV (Thermal Marking Velocimetry), and CFT (Controlled Flux Technique).

2.2.1 Particle Image Velocimetry

Particle image velocimetry is an optical method of flow visualization to obtain instantaneous velocity measurement.

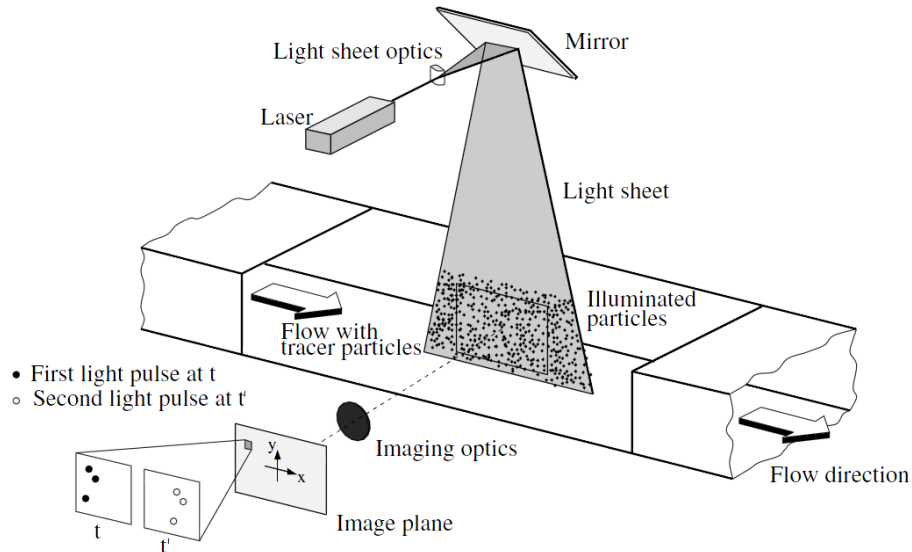


Figure 2.4: Experimental arrangement for particle image velocimetry (Raffel et al., 2013).

PIV is based on pictures of tracers illuminated by a laser light sheet. The experimental setup of a PIV system typically consists of several subsystems. In most applications tracer particles have to be added to the flow. Those particles are small enough, and with properties similar and match to the fluid, such that the particles are assumed to follow the flow accurately without overly disturbing the flow. Ideal particles have the same density as the fluid. By taking a rapid series of pictures illuminated by the laser light, the displacements of particles can then be used to obtain velocity maps of the fluid.

The tracer particles are usually be of the order of 10 to 100 micrometers.

Figure 2.4 briefly sketches a typical setup for PIV recording in a wind tunnel. Small tracer are added to the flow. A plane (light sheet) within the flow is illuminated twice by means of a laser (the time delay between pulses depends on the mean flow

velocity and the magnification of imaging). The light scattered by the tracer particles is recorded through a high quality lens either on a single frame (e.g. on a high-resolution digital or film camera) or on two separate frames.

The Figure 2.5 indicates in a very short period of time, usually smaller than $100\mu s$, we tracked the particles so that in a specific area, we can use cross correlation method to analyze the data. The PIV program uses 2D cross-correlations between images at times t and $t+\Delta t$ to determine displacement between two pictures. In each frame, sub-images are chosen (samples in Figure 2.5), cross correlations between the two samples give the most likely particle displacement during the Δt time interval. For each pair of images, one velocity vector is estimated by finding the maximum of the cross-correlation.

The operation is repeated for samples or sub-windows covering the whole image footprint. PIV is performed in three different configurations: with the final 2D velocity map oriented in a vertical longitudinal plane, vertical transverse plane and horizontal plane.

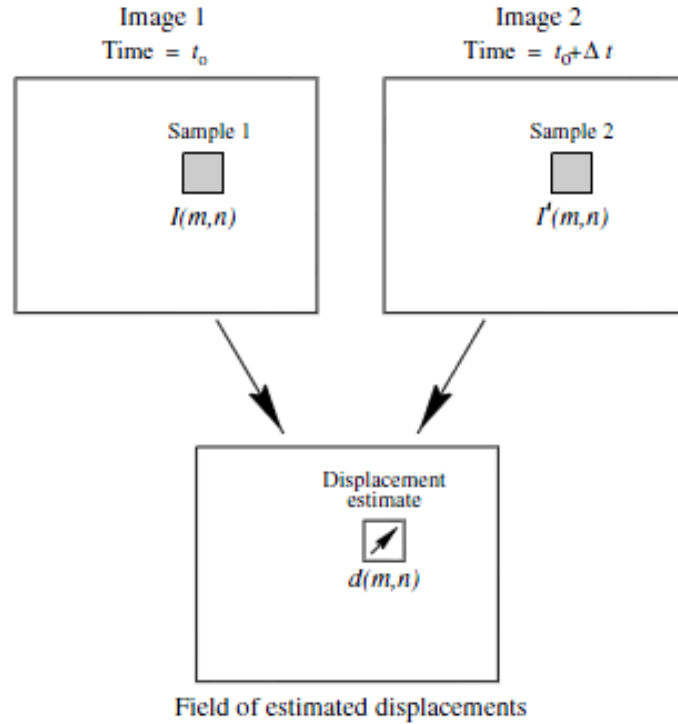


Figure 2.5: Conceptual arrangement of frame-to-frame image sampling associated with double frame/single exposure Particle Image Velocimetry (Raffel et al., 2013).

2.2.2 Thermal Marking Velocimetry

Thermal Marking Velocimetry (TMV) is an active infrared thermal imaging technique, which was first developed by Veron and Melville (2001) and subsequently used in many projects like Veron et al. (2008) and Savelyev et al. (2013).

The basic premise of Thermal Marking Velocimetry is to use active infrared heated spots on the water surface to track, visualize and quantify the surface flow. Those spots are used as passive Lagrangian markers (Veron et al., 2008). It is similar, in principle, to particle image velocimetry (PIV) but is Lagrangian in nature (Raffel et al., 2013). The added benefit of the TMV method is that the temperature, and temperature decay rates of the heat marker can also be used to estimate the surface heat flux.

In the project, the laser marker is programmed to lay down complete patterns

of 16 heat spots at a 0.48 Hz repetition rate yielding 28.8 complete patterns every minute. At very low wind speeds, spots can remain visible and detectable by the infrared camera for 2 seconds. The displacement of heat spots between consecutive image pairs gives an accurate measurement of the average Lagrangian water surface velocity and its spatial and temporal derivatives. Each spot is tracked individually until it leaves the field or decay to the background temperature.

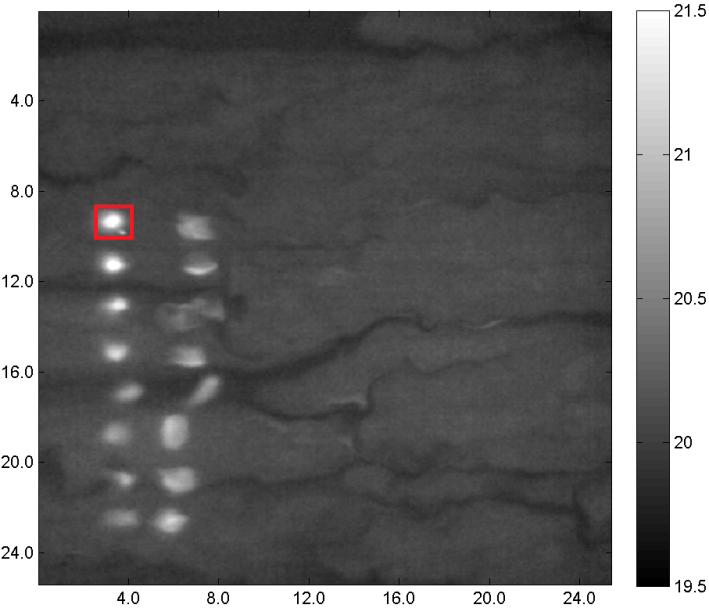


Figure 2.6: An example of a surface temperature image when active heat dots are visible using TMV, the wind is going from left to right in these infrared images.

Figure 2.6 is an example of the surface temperature, the grayscale represents the temperature where black is cold and white is warm. The highlighted spot in the figure indicates the spot that is tracked individually. In Figure 2.6, the 16 spots are tracked individually to obtain the averaged velocity of the water surface by TMV.

2.2.3 Controlled Flux Techniques

The Controlled Flux Technique (CFT) was first put forward by Jain (1989) in 1989 and further refined by his group. Since then, CFT was applied and developed in many other studies like Veron and Melville (2001), Zappa et al. (2001), Asher et al. (2004), etc. Scientists can use a high-resolution thermal imager (in the project we used infrared cameras) to track the thermal marker on the water surface as well as its temperature evolution.

The principle of CFT is to use a thermal marker on the water surface and apply the high-resolution thermal imager to track the temperature time evolution by the thermal marker (it is the CO_2 laser in the project).

Directly beneath the surface is a thin viscous sublayer. There is an analogous thermal sublayer within the viscous sublayer which is because of the difference between kinematic viscosity and thermal diffusivity is around one order of magnitude. At the air-sea interface, the thermal sublayer is usually $O(0.01 - 1)$ mm. The surface temperature (skin temperature), T_{skin} is usually a few tenths of a degree cooler than the temperature beneath the surface $T_{subskin}$ (subskin sea surface temperature).

The diffusion equation at the temperature spot is

$$\frac{\partial \Delta T(x, y, z, t)}{\partial t} = \kappa \nabla^2 (\Delta T(x, y, z, t)) - \frac{1}{t_*} \Delta T(x, y, z, t) \quad (2.1)$$

κ denotes the diffusion coefficient for heat in water, $\Delta T(x, y, z, t) = T(x, y, z, t) - T_{subskin}$ as the temperature difference is the surface temperature to subtract a constant subskin temperature. t_* is the mean surface renewal time and we have the surface renewal rate as decay rate:

$$\lambda = t_*^{-1} \quad (2.2)$$

The initial temperature distribution generated by CO_2 laser satisfies Gaussian equation, we have $\Delta T(x, y, z, 0) = T_0 e^{-(x^2+y^2)/\sigma^2} e^{z^2/h^2}$ where σ is the size of the heat spot and the center of the spot is regarded at $(x, y) = (0, 0)$.

With $T(z, t) = \iint T(x, y, z, t) dx dy$, as a result, equation 2.1 can be reduced to

$$\frac{\partial \Delta T(z, t)}{\partial t} = \kappa \frac{\partial^2 \Delta T(z, t)}{\partial z^2} - \frac{1}{t_*} \Delta T(z, t) \quad (2.3)$$

For Equation 2.3, we have a simple solution for the spot temperature at the water surface can be obtained:

$$T(0, t) = T_0 \frac{h}{\sqrt{h^2 + 4\kappa t}} e^{-t/t_*} + T_{subskin} \quad (2.4)$$

According to Equation 2.4, the decay rate t_* can be obtained from the observed decay (rate) of the spot temperature.

Once the decay rate is obtained, combined with Danckwerts's equation of surface-age distribution function as well as Veron et al. (2011)'s extended the equation into heat problem,

$$k_H = \frac{j_H}{\rho C_p \Delta T} = \sqrt{\kappa \lambda} \quad (2.5)$$

Equation 2.5 indicates the relationship of the renewal rate and the heat transfer velocity k_H , where κ is the molecular diffusivity of heat.

Veron et al. (2011) assumed a Fickian diffusion law to relate the mean surface temperature difference $\overline{\Delta T_0}$ with the mean net flux of heat Q .

$$|\overline{Q}| = k_H \rho_w C_p |\overline{\Delta T_0}| \quad (2.6)$$

ρ_w is the water density, C_p is the specific heat capacity of water, and $\overline{\Delta T_0}$ is the mean temperature difference across the thermal diffusive layer, that is, the temperature difference between the subskin and skin. The overbars mean the averaged value.

In short, the Fickian diffusion law shows the relationship between the heat flux and the temperature gradient.

In order to get renewal rate λ , we know that, since the surface renewal is mainly caused by the turbulent eddies. Direct measurements of the renewal/decay rates usually require active infrared methods. For measurement, infrared remote sensing is the best

way up to date. We used infrared cameras to track the dots, which are the spots we used the laser to heat the surface. The dots are indicated in the Figure , the figure 3.3 indicates the temperature of the water surface and the red box emphasized the spots heated by the laser.

Figure 2.6 also indicates the CFT method, we tracked not only the velocity of the spots but also the temperature diffusion of the spots to obtain the heat flux.

Heat is an ideal tracer for air-sea gas transfer (Schimpf et al., 1999). The heat transfer velocity can be calculated by Equation 2.5 and the gas transfer velocity can be measured by

$$\frac{k_g}{k_h} = \left(\frac{S_{c_h}}{S_{c_g}}\right)^n \quad (2.7)$$

with the Schmidt number S_{c_h} (heat) and S_{c_g} (gas) and the Schmidt number exponent n . n usually is a parameter between 1/2 and 2/3 depending on the friction velocity and the mean square slope of the waves. If we use a ± 0.02 uncertainty for n and a relative error of the diffusion coefficient κ of 5%, the maximum absolute error of the gas exchange rate calculated from the heat transfer is around 12%. Also, the gas transfer and flux have been stated in Ward et al. (2004)

The large difference in the Schmidt number (7 for heat, 600 for CO₂).

Chapter 3

RESULTS

The work presented in this chapter was conducted jointly with Marc Buckley and Fabrice Veron in the Air-sea Interaction Laboratory in the University of Delaware in Lewes. Marc Buckley and Fabrice Veron performed the experiments and the author participated in the data analysis.

In this chapter, we describe the results of the laboratory experiments performed at multiple wind speeds and accelerations. In most of this chapter, the case with the highest wind acceleration and speed will be shown for illustration purpose but all data were analyzed. Summary tables and figure are presented when appropriate.

3.1 Waves and Winds

3.1.1 Winds and wave height

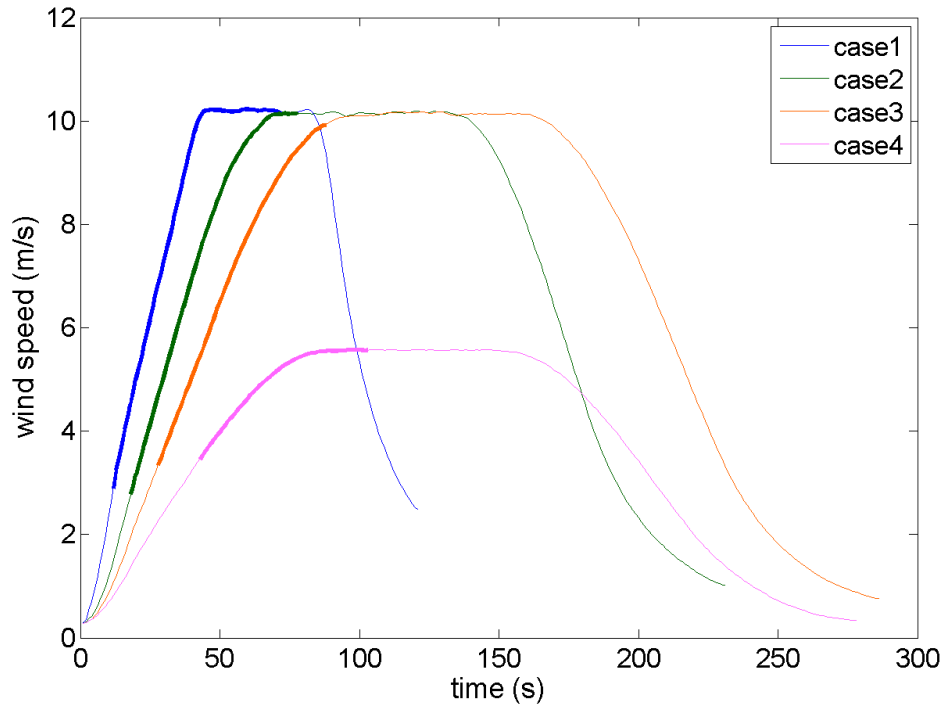


Figure 3.1: Time series of the wind speed for the four cases. Also shown are the four recording time for the Infrared Cameras and PIV cameras. The wind speed before it reaches to the final highest speed matches the equation 3.1 for each case.

In these experiments, the wind is started from rest over a quiescent water surface. Several wind speed/acceleration combinations are studied. Figure 3.1 are the time series of the wind speed of the four cases studied here. We also show the data acquisition time (60 s for each case) for the Infrared cameras and PIV cameras. The infrared and PIV cameras started to acquire data at different time depending on experimental conditions in order to capture the formation of the LC. Start times were $t = 12s$ for the first case, $t = 18s$ for the second case, $t = 28s$ for the third case, and $t = 43s$ corresponds to the final case. Each case lasts 60 s for image recording.

For the first three cases, we have the same final wind speed of approximately $10.20m/s$ and different wind acceleration, while the fourth case is with lowest final

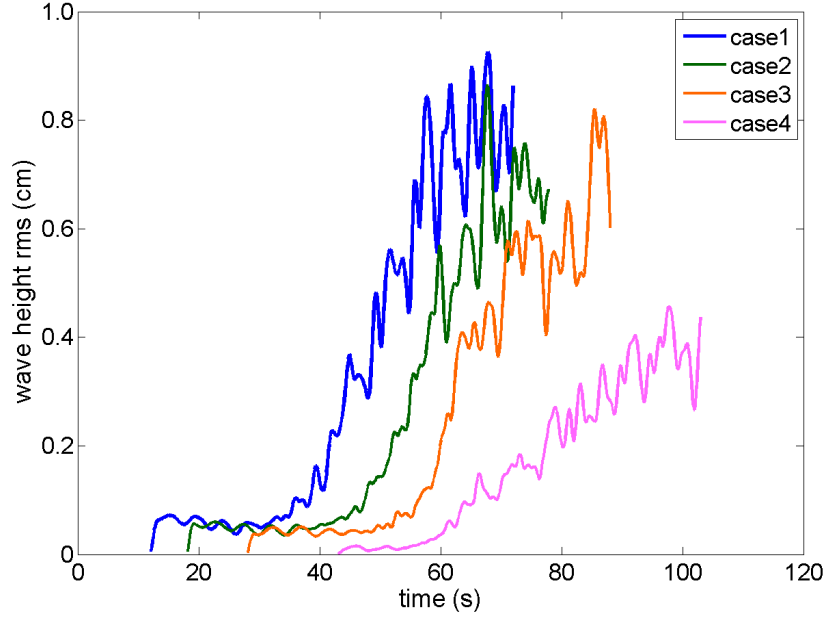


Figure 3.2: Wave height rms for the four cases.

wind speed of $5.56m/s$, and lowest acceleration. Since the evolution time of LC is before the wind speed reaches its final speed, we can ignore the influence of final wind speed and only focus on the influence of wind acceleration.

We set $t = 0s$ as the time when the wind starts to blow over the water. In the four cases, before it reaches the final highest speed, the wind speed follows a linear relationship with a constant acceleration.

$$\begin{aligned}
 v &= 0.25t; \\
 v &= 0.19t; \\
 v &= 0.14t; \\
 v &= 0.08t;
 \end{aligned}
 \tag{3.1}$$

v is the wind speed (m/s), t is the time (s).

Figure 3.2 shows the root mean square of wave height for each case. The wave gauge recorded 60 seconds for each case, according to the highlighted time for in Figure 3.1.

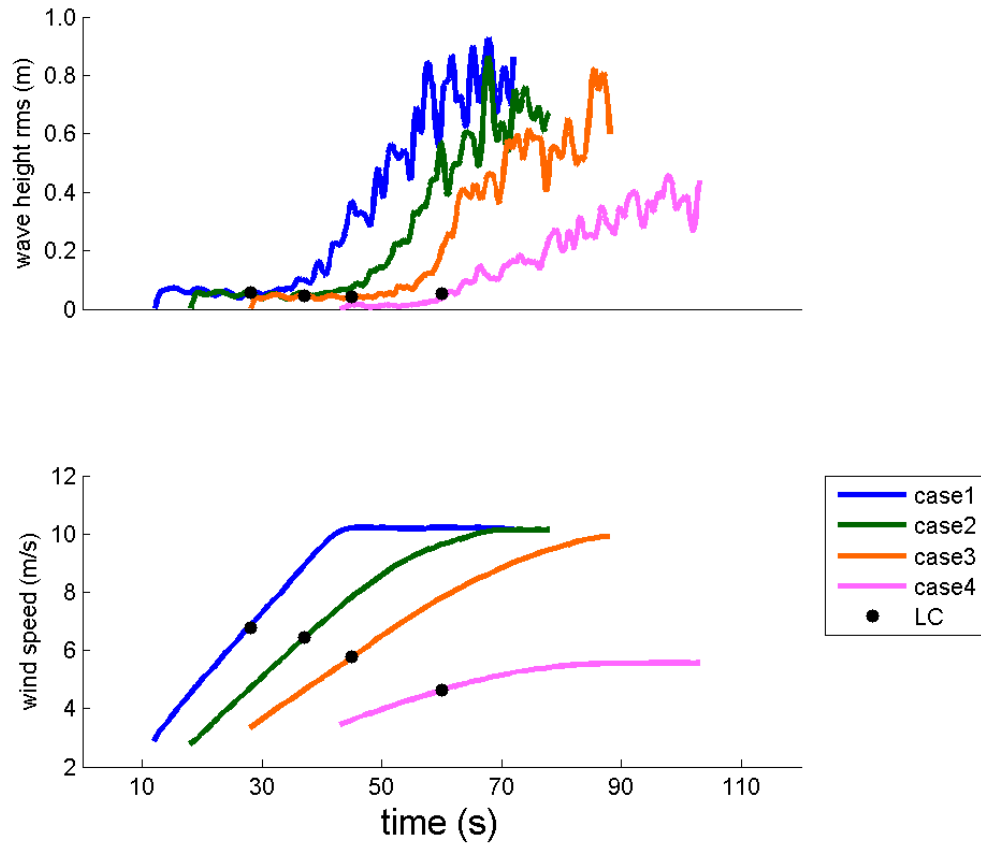


Figure 3.3: Time series of the wind speed for the four cases. Black dots indicate the evolution time of LC for each case

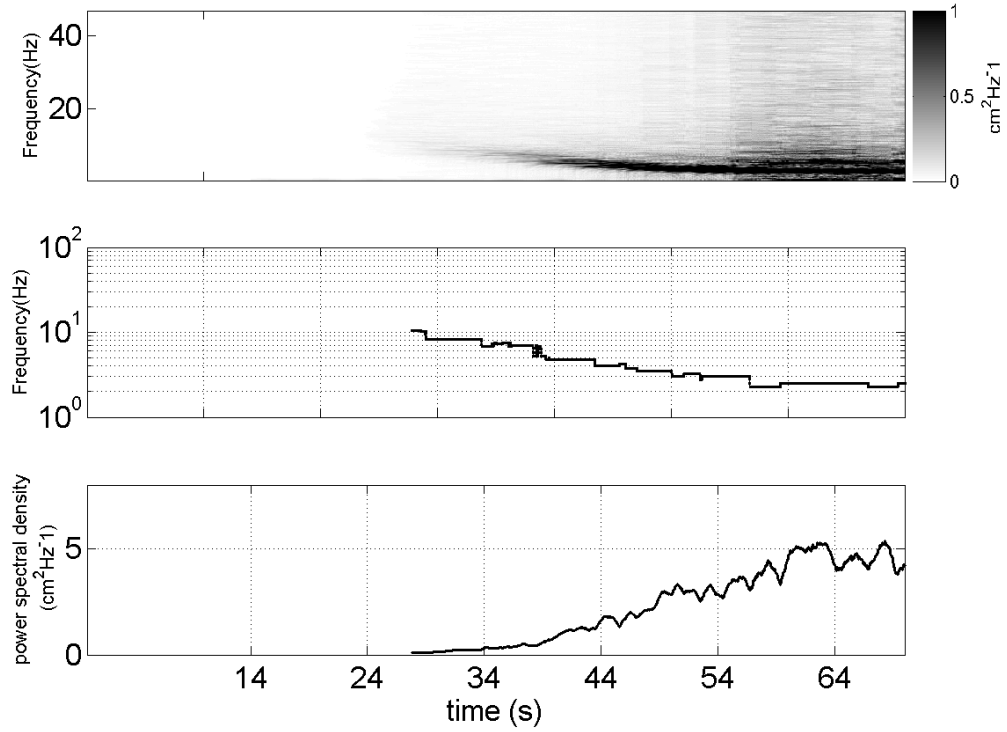


Figure 3.4: (a) is the wave spectrogram of surface displacement recorded by the wire wave gauge for a final wind speed of 10.2m/s for Case 1. (b) is the time evolution of the peak frequency. (c) is the the peak energy density.

Figure 3.3 is the comparison of rms wave height and wind speed. The black dots marked here are the time when we observed the LC inception as $t = 29\text{s}$, $t = 37\text{s}$, $t = 46\text{s}$, and $t = 60\text{s}$.

3.1.2 Wave spectrum

Figure 3.4 is the wave spectrum, peak frequency, and peak energy density of Case 1. Figure 3.4(a) is the wave spectrum of surface displacement recorded by the wire wave gauge for a final wind speed of 10.2m/s and acceleration of 0.25m/s^2 of Case 1. Figure 3.4(b) is the time evolution of the peak frequency. Figure 3.4(c) is the the peak energy density. Figure 3.4 shows the time we first detected the waves and their evolution.

The wave spectrogram in Figure 3.4 was calculated using a 4 seconds window.

The first detectable waves appear at around 28.5s with the frequency of 7.9 Hz, and shortly after, the LC appears. Different cases will be summarized in Table 3.1.

3.1.3 Initial scales of winds and waves

As seen in the previous section, both the wind and waves grow with time. Table 3.1 indicates the different statistical parameters of winds and waves for each case and the initial wave parameters for the first detectable waves as time t_w , phase speed c_w , rms_w , wind speed v_w , frequency f_w , wavelength λ_w , wave number k_w .

The dispersion relationship of linear capillary-gravity surface-wave (Pijush K. Kundu, 2012) is

$$\omega = \sqrt{k\left(g + \frac{\sigma k^2}{\rho}\right) \tanh(kH)} \quad (3.2)$$

so the phase velocity is

$$c = \sqrt{\left(\frac{g}{k} + \frac{\sigma k}{\rho} \tanh kH\right)} \quad (3.3)$$

where $\tanh(2\pi H/\lambda) \approx 1$ has been applied.

3.2 Surface Thermography—Passive Infrared Imaging

Table 3.1: Summary of wind and wave statistical parameters of the four cases

Case	Wind acceleration (m/s^2)	Final wind speed (m/s)	Time t_w (s)	Phase speed c (cm/s)	rms_w ($10^{-4}m$)	Wind speed v (m/s)	Frequency f_w (Hz)	Wavelength λ_w (cm)	Wave number k_w (m^{-1})
1	0.25	10.20	28.50	23.96	5.73	7.26	9.47	2.53	247.98
2	0.19	10.20	34.50	23.53	3.66	6.11	10.41	2.26	277.61
3	0.14	10.20	44.50	24.60	4.01	5.81	8.60	2.86	219.44
4	0.08	5.56	59.50	26.71	3.30	4.66	7.03	3.80	165.78

The infrared camera was used to measure the surface temperature of the skin layer. Surface thermography was used in two modes: passive where the surface temperature patterns were used to image the LC and their evolution, and active where a CO₂ Laser was used to lay down Lagrangian heat markers.

3.2.1 Flow Visualization

There are four stages in the development of the surface flow and the LC when both wind and water start from rest.

1. The wind accelerates the surface also starts to accelerate under the effect of the wind shear stress.
2. Wind waves are formed.
3. LC appears and starts the transition to turbulence.
4. Flow evolves to fully developed turbulence.

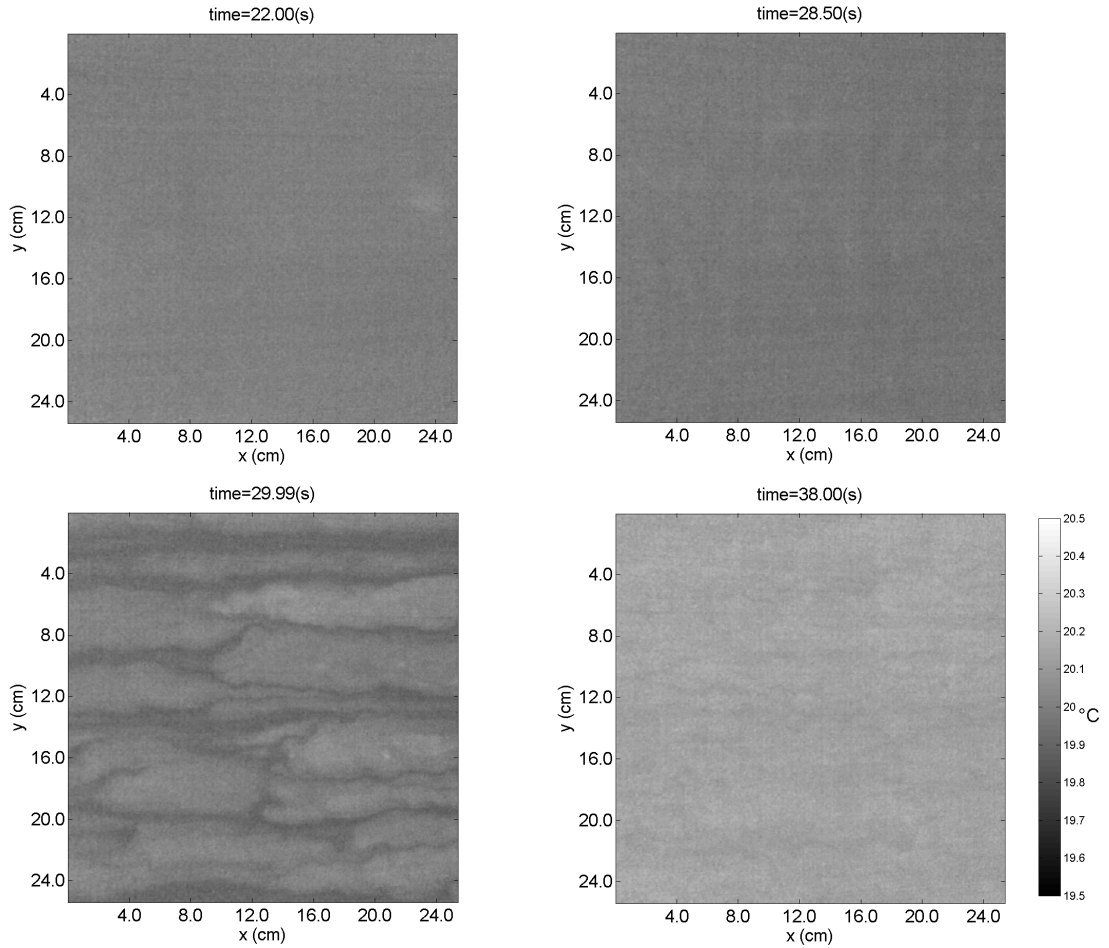


Figure 3.5: Evolution of the temperature surface flow of the Case 1 — the four stages mentioned in the section. The four figures show the time evolution of the surface flow of the four stages. x is the direction of the flow while y is the cross-wind direction. The temperature is given by the colorbar.

Figure 3.5 is a series of temperature image of the water surface. According to the four flow stages, we set $t=0$ s as the time when wind starts. We identified $t=22.00$ s, 28.50 s, 29.99 s, 38.00 s as the times when the flow was in different flow stage: At $t=22.00$ s, the wind was blowing over the water surface, and the water surface started to accelerate because of the wind shear stress. The water surface was moving downstream as some momentum from the wind was transferred to the water surface layers. A subsurface laminar shear layer developed.

At $t=28.50$ s, from the wave gauge as well as the infrared cameras, the waves just were formed.

At $t=29.99$ s, the LC was just about form and upwelling (warm water from below the cool skin) was clearly visible on the image. Shortly after, the LC were clearly apparent on the IR images. The flow then started the transition to turbulence.

At $t=38.00$ s, the flow was fully turbulent and longer waves had developed. The temperature of the surface is slightly higher now that the turbulence has essentially destroyed the cool skin (the molecular thermal layer).

At the early stage of the flow. Viscous diffusion is playing an important role, it transfers the momentum to depth and a laminar boundary layer develops. Figure 3.6 shows the evolution of the flow and the LCs inception in case 1.

Figure 3.6 is a 2.5 seconds time series of flow visualization showing the evolution and development of the centimeter scale LC at final wind 10.2 m/s and acceleration 0.25 m/s^2 . The LC started at around 29 s and was developed since then and turned into full turbulence after 31 s.

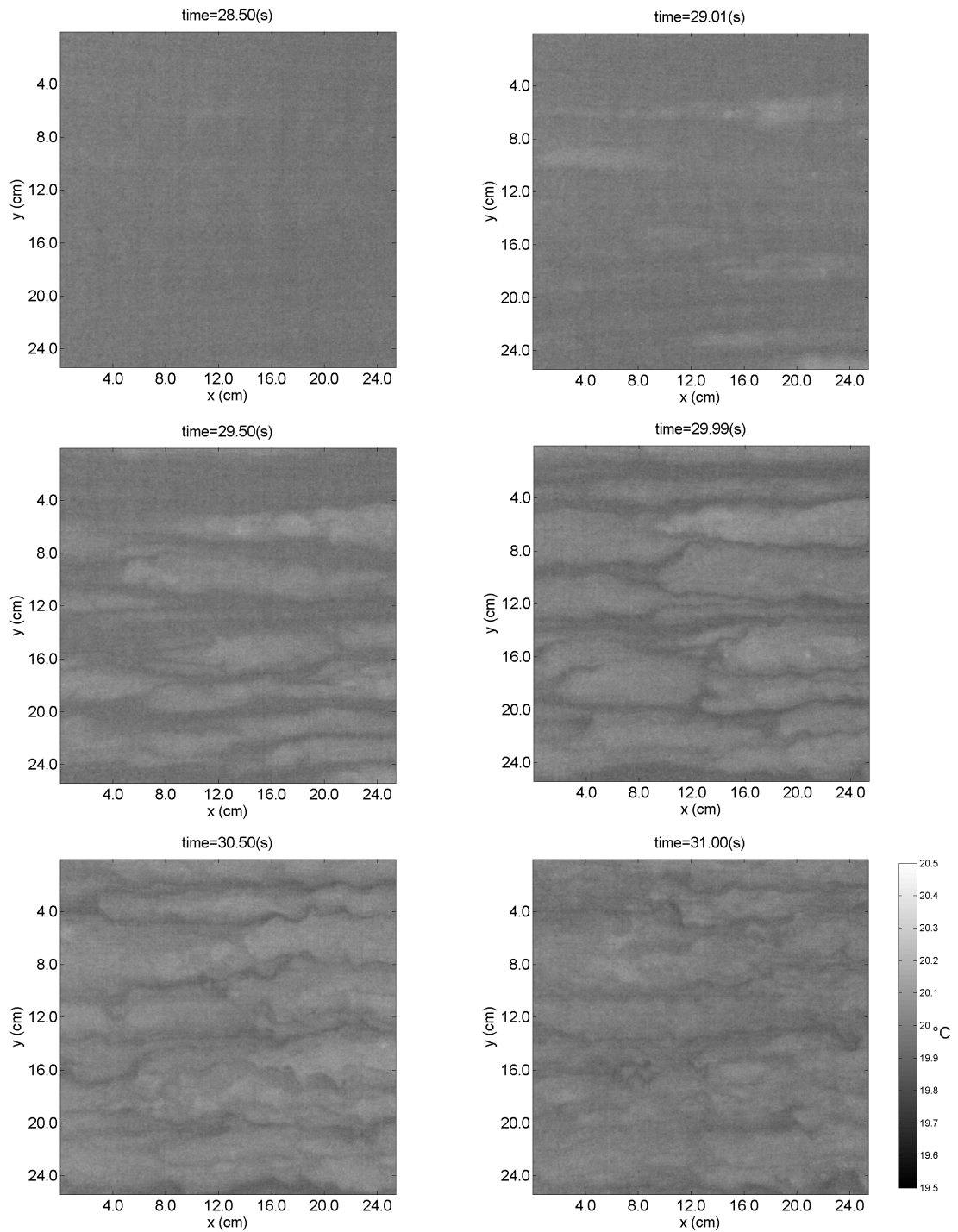


Figure 3.6: Infrared images showing the development and evolution of LC imaged by the surface temperature as a function of time for Case 1. Images sizes are 24.7 cm \times 24.7 cm. The wind is blowing from left to right. Time shown since the inception of the wind are from 28.5-31s from the start of the wind, in 0.5s increments. The temperature is given by the colorbar.

Figure 3.6 is an example of Case 1 showing how the surface flow and LC developed and evolved. The four cases studied here show a similar evolution of the development of the LC, with however, time and length scale differences. Figure 3.7 for example shows the LC (surface temperature images) at the same stage of the development of the LC. See for example the difference in length scales between case 3 and 4.

Table 3.2 summarizes the time and length scale of the inception of the LC for the four cases.

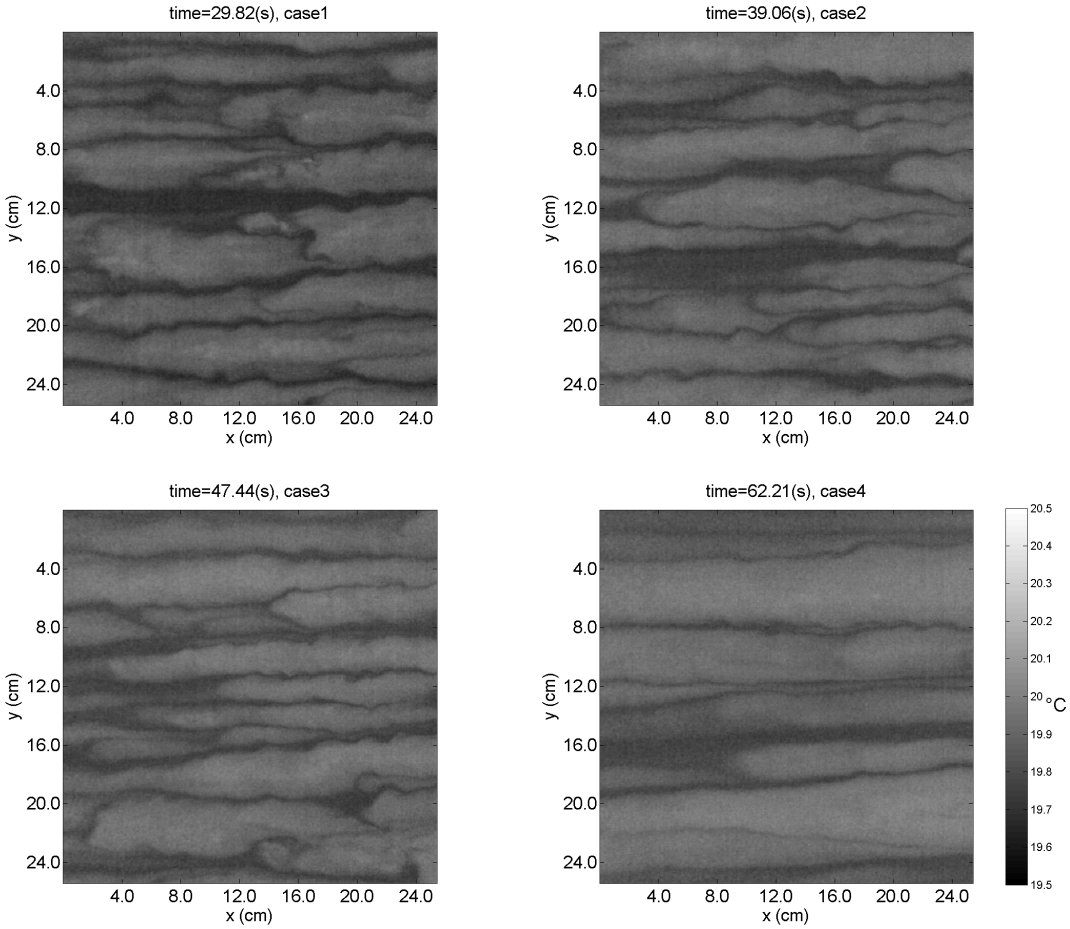


Figure 3.7: The surface temperature field showing the LC for the four cases.

Table 3.2: Summary of the time and length scale of the inception of the LC.

Case	LC inception time (s)	Time length of LC (s)	Row spacing (cm)	Wind speed v_{LC} (m/s)	wave height rms_{LC} ($\times 10^{-4}$ m)	wave number k_{LC} (m^{-1})
1	28.48	2.36	4.32	7.15	5.42	136.89
2	36.77	3.53	4.72	6.45	5.36	135.05
3	45.30	2.50	4.86	5.77	4.38	96.56
4	60.42	3.09	5.83	4.65	6.89	56.12

3.2.2 Statistics of the Flow

3.2.2.1 Temperature Standard Deviation

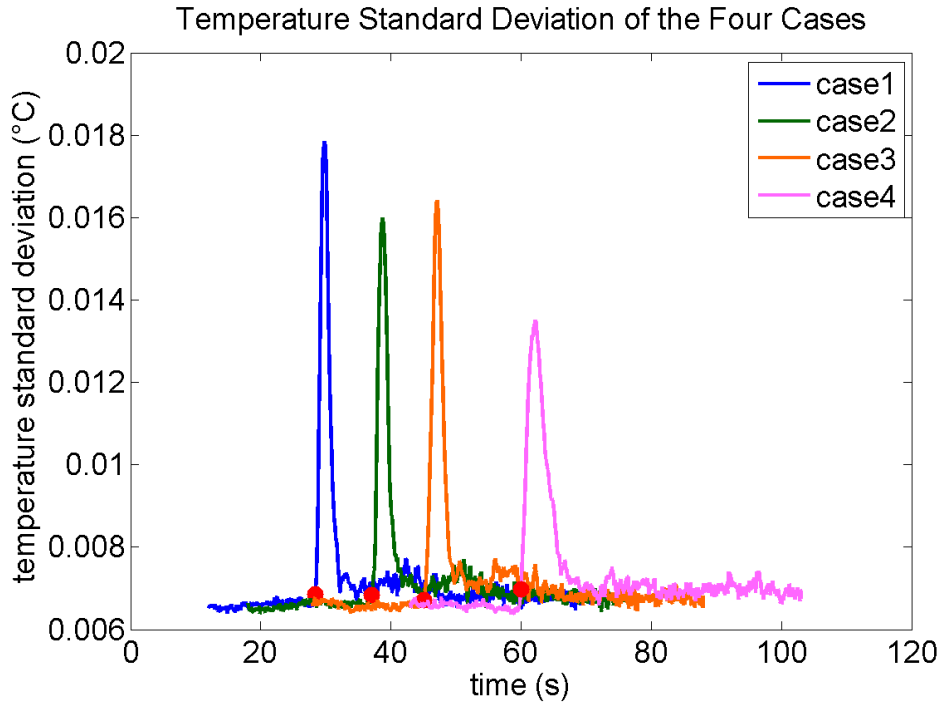


Figure 3.8: Normalized standard deviation of the highpass temperature, α , for the four cases. The red dots in the figure are the LC inception time.

In order to minimize some of the noise inherent in the IR measurements, here, we have highpassed the temperature measurements.

The standard deviation of the high-pass temperature is noted α . The black dots in Figure 3.8 are the time inception of LC.

From Figure 3.8, we can see that the inception of the LC, marked with a red dot, coincides with a rapid and sudden increase of α . Also, the maximum alpha increases with increasing acceleration of the flow.

After the LC has transitioned to fully developed turbulence, α returns to a value close to that before the inception of the LC. We suggest here that α could serve as a good indicator of the LC transition and relative intensity of the inception of the LC.

Besides, the time length scale of LC (defined as the time between the inception and the time at which the flow becomes turbulent) is longer with smaller wind acceleration. For example, the LC appear relatively stable for up to 8 seconds in Case 1, and the transition to full developed turbulent occurs only 4 seconds after the inception of the LC in Case 4.

Table 3.3 is the summary of the statistical parameters of the surface temperature related to the normalized highpass temperature standard deviation. We measured the highest temperature standard deviation, the temperature standard deviation before and after LC inception, and its ratio to the highest standard deviation, the time period between the LC inception to the time when the flow becomes turbulent.

Besides, the ratio of the highest α (at the LC inception time) to the α before LC and after LC can also be an indicator of the development and evolution of LC. The ratios of Case 4 are the smallest among the four cases. We assumed that it was not only because of the wind acceleration but also the final wind speed.

The time period between the LC inception and the flow becomes fully turbulent in Table 3.3 matched the time period what we observed the LC in Table 3.1.

As a conclusion, the temperature standard deviation as α helps give us a better idea on the time scale length and the development and evolution of the LC. It also appears that the acceleration, rather the speed per say, plays an important role in determining the time and length scales associated with the inception and development of the LC.

Table 3.3: Summary of standard deviation of the surface temperature measured by infrared camera.

Case	Highest α ($\times 10^{-4}$)	α before LC ($\times 10^{-4}$)	α after LC ($\times 10^{-4}$)	Ratio of highest α to α before LC	Ratio of highest α to α after LC	Time period (s)	Time length (s)
1	9.27	3.31	3.34	2.89	2.74	28.43-33.23	4.80
2	8.37	3.31	3.42	2.53	2.45	37.03-41.80	4.77
3	8.97	3.32	3.39	2.70	2.65	45.25-51.38	6.13
4	7.08	3.32	3.49	2.13	2.03	59.95-67.62	7.67

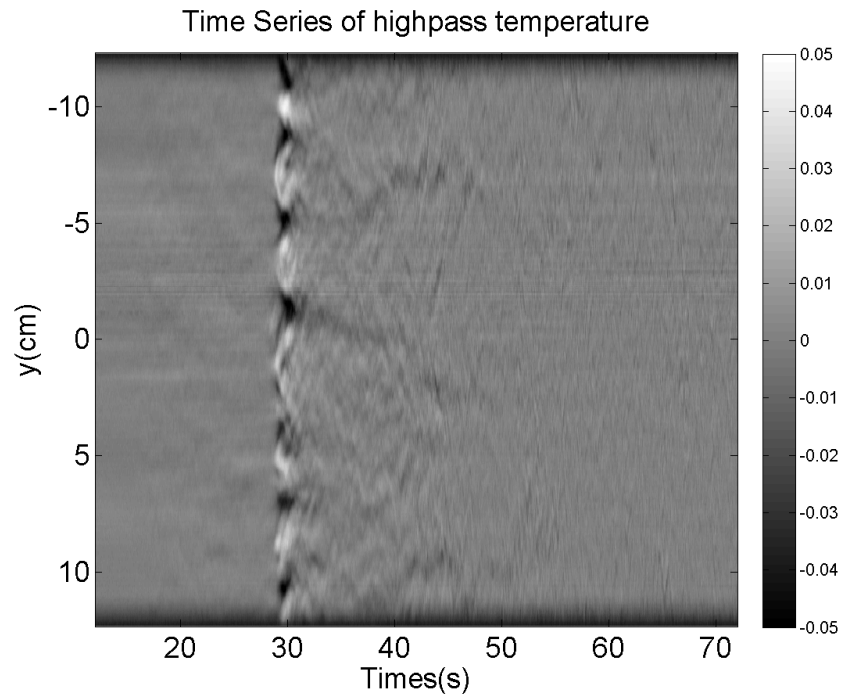


Figure 3.9: Time series of a cross-wind cut of the highpass temperature. The band at top and bottom of the figure is noise introduced by the camera lens.

3.2.2.2 Time Series of Mean Temperature

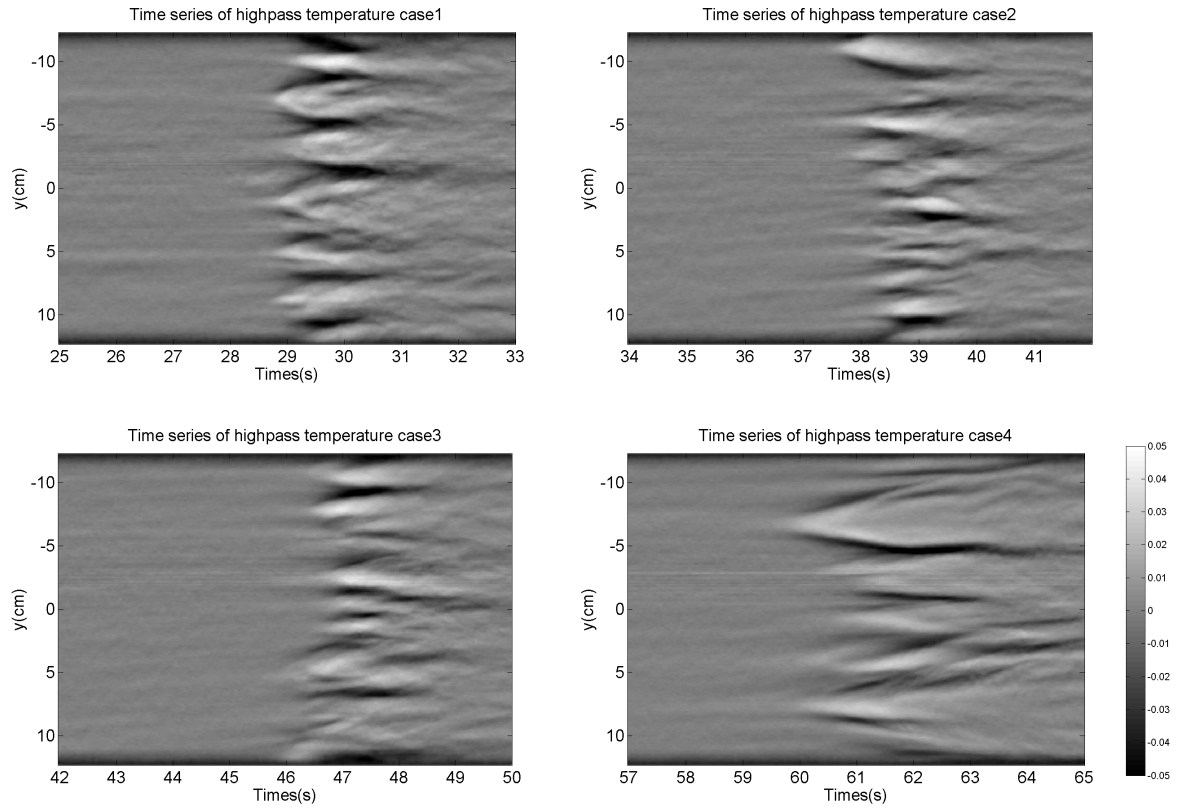


Figure 3.10: The time series of the mean temperature in the cross-wind cut with a 8-second time between before LC inception and turbulence of the four cases.

Figure 3.9 is the time series of a cross-wind highpass temperature cut. The time at which the instability is first observed as well as the length scale of the LC can be seen on Figure 3.9. It is apparent that the LC provides the transition to turbulence. Figure 3.10 is the time series of the mean temperature in cross-wind cut of the four cases. The row spacing in each case has been discussed in Table 3.3.

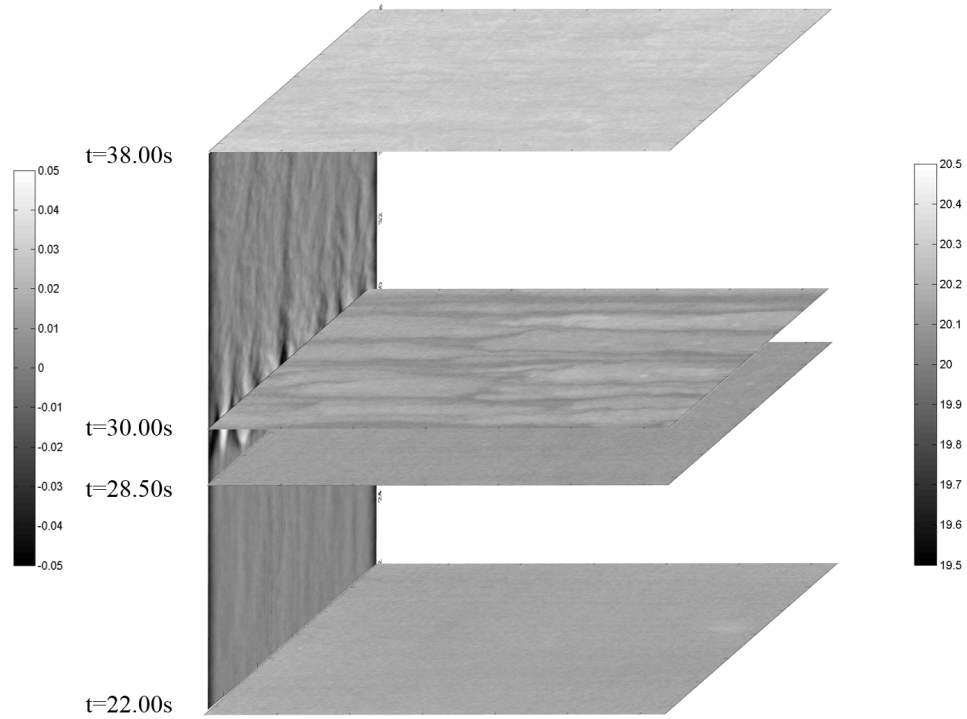


Figure 3.11: Three dimensional representation of the surface temperature. The horizontal images are the figure 3.6. The vertical image shows a highpassed temperature cross-wind cut though the surface images with time as figure 3.12. The colorbar in the left-hand side is the colorbar for the vertical image while the colorbar in the right-hand side is the colorbar for the horizontal images.

Figure 3.11 shows the three-dimensional representation of the surface temperature where x is the along-wind direction y is the cross-wind direction, and the vertical axis is the time. The time period of Figure 3.11 shows the four stages of the flow and how the LC develops during the time. From Figure 3.11, the LC scales grow from small to big, the row spacing between two rows also grows with the LC.

3.3 Surface Thermography—Active Infrared Imaging

In addition to the passive infrared temperature images of the water surface, the active infrared methods were also used in our experiments.

3.3.1 Velocity-Momentum Boundary Layer

We also performed experiments where we used a CO₂ laser to actively lay down heat markers on the surface with a pattern of 16 heat spots marked in the cross-wind direction. Complete patterns are laid down with a frequency of 1.8 Hz. These heat markers were used as Lagrangian surface markers and were detected with the infrared camera.

The heat spots have no influence on the dynamics at the interface. From the wavelength of the CO₂ laser, we anticipate that the heat penetrated only approximately 10-100 μm , thus, the heat markers are considered to be Lagrangian markers at the interface. Each spot is approximately 1.4 cm in diameter initially. We tracked the first 8 spots to retrieve the Lagrangian velocity and displacement of the interface.

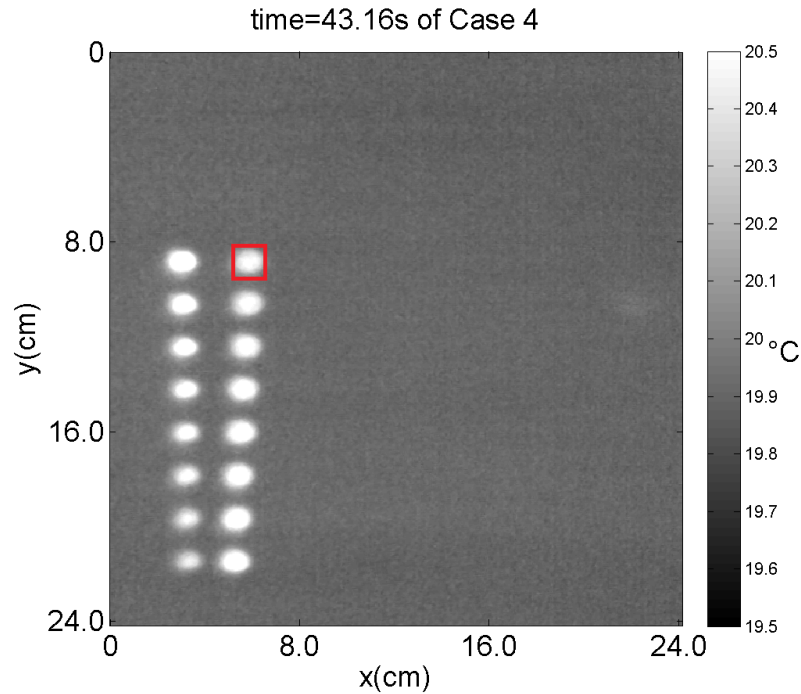


Figure 3.12: Heat spots example of a surface temperature image where active heat dots are visible.

Figure 3.12 is an example of Case 4 showing the surface temperature at time=43.16 s. The wind was along the x direction and the gray scale indicates the surface temperature in the area. The red area indicates the location of the one of the heat markers

laid down by the laser.

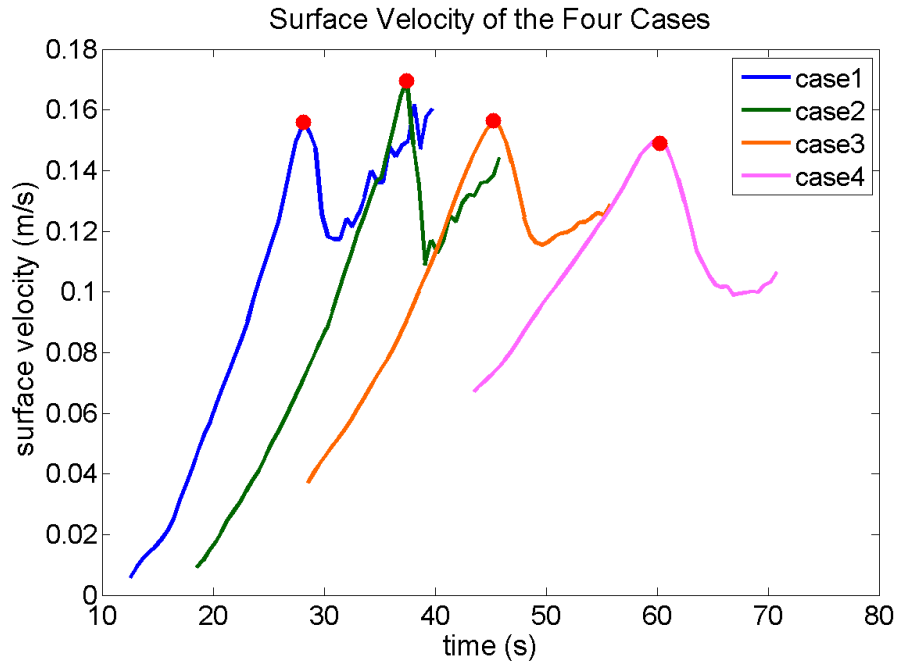


Figure 3.13: The surface velocity for the four cases. Different colors indicate different cases. Only 30 seconds of data around the inception of the LC are shown here. The red dots in the figure are the LC inception time.

Figure 3.13 shows the surface velocity for the four cases in the first twenty-eight seconds of the recording. The flow became turbulent after LC inception so that it's difficult to track the markers velocity in a way that is representative of the mean surface speed. The red dots in Figure 3.13 are the time when LC appear. From Figure 3.13, the LC inception time matches the maximum surface velocity. After the inception of the LC, the surface velocity diminishes. This is a result of the LC which efficiently mix the momentum that was initially imparted to the surface laminar boundary layer.

Meanwhile, the velocity for each case also exemplify the four stages of the flow. The surface accelerated; reaches maximum velocity when the LC appear; the LC transfer surface momentum to depth reducing the surface velocity; and the surface flow becomes fully turbulent. Here, after the flow has become turbulent. the interface appears to continue to accelerate somewhat, perhaps under the influence of the wind

stress which continues to increase. Table 3.4 summarizes the results of the surface velocity for the four cases.

Table 3.4: Summary of Surface Velocity of the Four Cases.

Case	Max Velocity (cm/s)	Velocity acceleration before LC (cm/s)	Time of instability (s)
1	15.59	1.34	28.96
2	16.97	1.20	37.44
3	16.00	0.82	45.22
4	15.19	0.58	60.22

In addition to the surface parameters provided by the momentum and thermal data, the wave gauge provided the surface-wave parameters at the inception of the LC. Table 3.5 summarizes the results.

Table 3.5: Measured surface wave parameters at the inception of the LC of the four cases.

Case	Wavelength λ_{LC} (cm)	Frequency f_{LC} (Hz)	Wave number k_{LC} (m ⁻¹)	Phase velocity c_{LC} (cm/s)
1	2.28	10.33	87.55	23.59
2	3.42	7.56	183.72	25.82
3	2.88	8.56	218.17	24.66
4	3.00	8.31	209.44	24.89

3.3.2 Thermal Boundary Layer

By tracking the dots, not only can we get the surface velocity but also we can retrieve the temperature decay rate. The decay rate is proportional to the heat flux,

this will discuss it in details in next chapter.

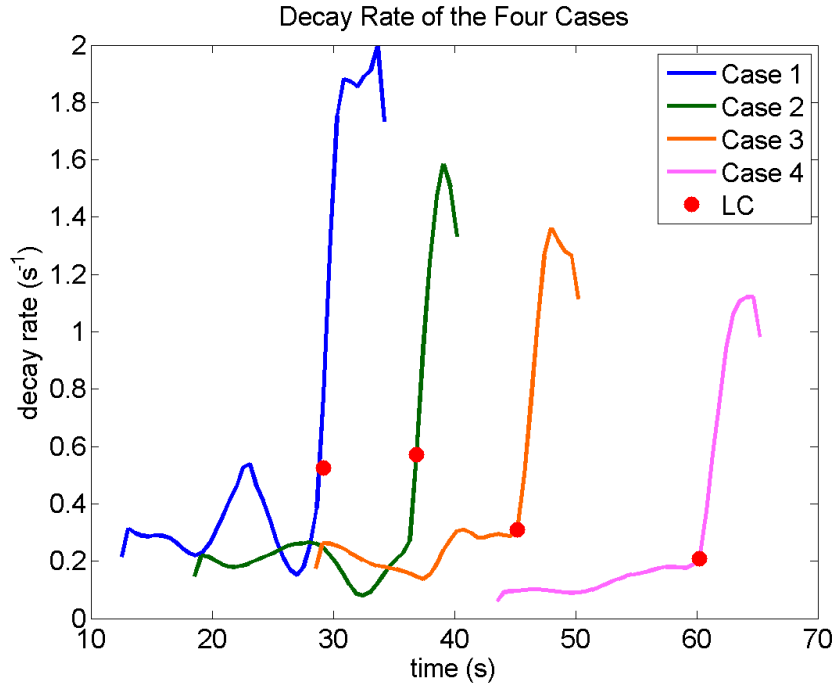


Figure 3.14: Decay rate of the heat markers for the four cases.

From Figure 3.14 and Table 3.6, we see the decay rate was clearly stable along with the wind acceleration before LC. When LC appear, the heat spot decay rates increase indicating that the LC enhance the heat transfer across the thermal boundary layer.

The maximum decay rate for each case, as in Table 3.6, is decreasing with the lower wind acceleration and speed.

Through the decay rate, we can calculate the heat transfer velocity as well as the gas transfer velocity, which would be talked in the next chapter.

According to our findings in previous sections, combined with the surface velocity, temperature standard deviation, ratio of the maximum to mean temperature. It is clear that the inception of the LC coincides with the laminar turbulent transition and with an enhanced surface heat flux.

Table 3.6: Summary of Decay Rate.

Case	Max decay rate (s^{-1})	Max decay rate time (s)
1	2.45	30.89
2	1.88	39.11
3	1.74	48.00
4	1.34	64.67

3.4 Subsurface Statistics Measurements

The Particle Image Velocimetry (PIV) and Laser Induced Fluorescence (LIF) are the techniques to measure and detect the subsurface water movement.

With this setup, the data obtained with the PIV are 2D maps of 2D velocity vectors (vertical and cross wind direction) in a vertical plane perpendicular to the direction of the wind. (see figure 2.1 for a sketch of the setup)

3.4.1 Cross-wind Direction

3.4.1.1 LC's evolution

Figure 3.15 is a series of the LIF images of the LC inception from 28.20 s to 31.44 s. The light gray underwater is dye that was placed on the surface and which is entrained by the LC.

It can be seen that the LC first occur around 29 s, which is also the time where the maximum surface velocity is observed (Table 3.4). It is concluded that the LC inception transfer the momentum to depth. The LC clear appear as pairs of counter rotating vorticies that bring surface water to larger depth, thereby distributing the momentum that was originally imparted to the surface by the wind.

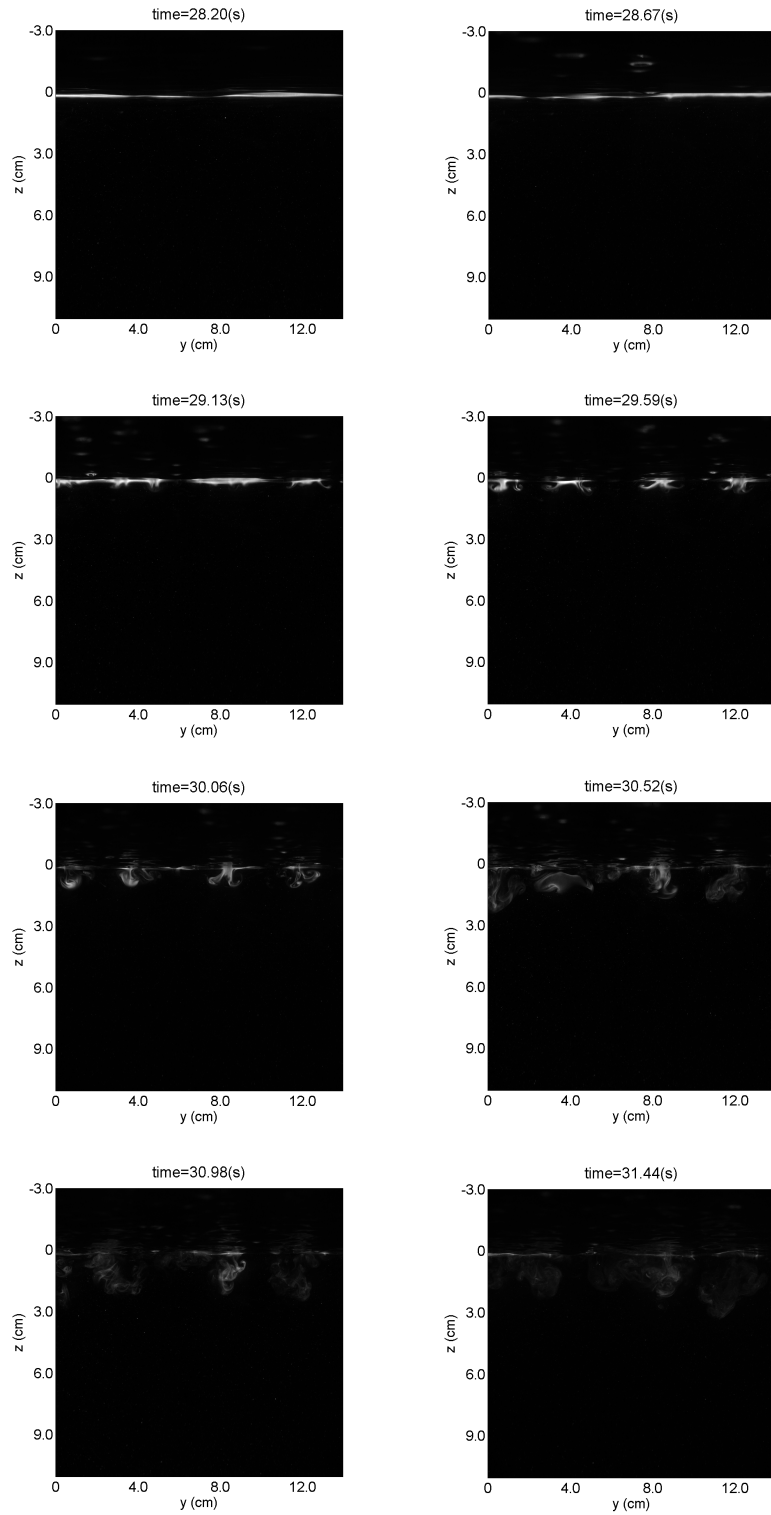


Figure 3.15: The inception and evolution of LC in cross-wind direction for Case 1, the gray scales in the figure is fluorescent dye in the water, which has no influence on the dynamics.

The LC evolve over a short period of time. From Figure 3.16 we can see the LC's inception has just started around 29 s. Then the LC become "fully formed" at around 30 s and started to break down from the "full cells" structure shortly after at around 31 s. Also from the infrared images in Figure 3.7, the "white streaks" which are the most prominent and visible characteristic of LC were still visible on the surface at around 31 s even though the "full cell structure" of the LC may be broken down under the water surface at that time.

3.4.1.2 Velocity in horizontal and vertical direction

The PIV data can also help us examine the structure and evolution of the LC. Since the PIV data provided the water velocity both in horizontal and vertical direction, the velocity can help us identify LC. Figure 3.16 shows a time series from 28.25 s to 31.44 s of the vertical velocity, while Figure 3.17 shows a time series of from the same time period of the horizontal velocity of the fluid. Compared with Figure 3.16 it is very clear that the LC enhance the vertical velocity. It looks like the velocity associated with the LC first originates from the surface; then penetrates the water column.

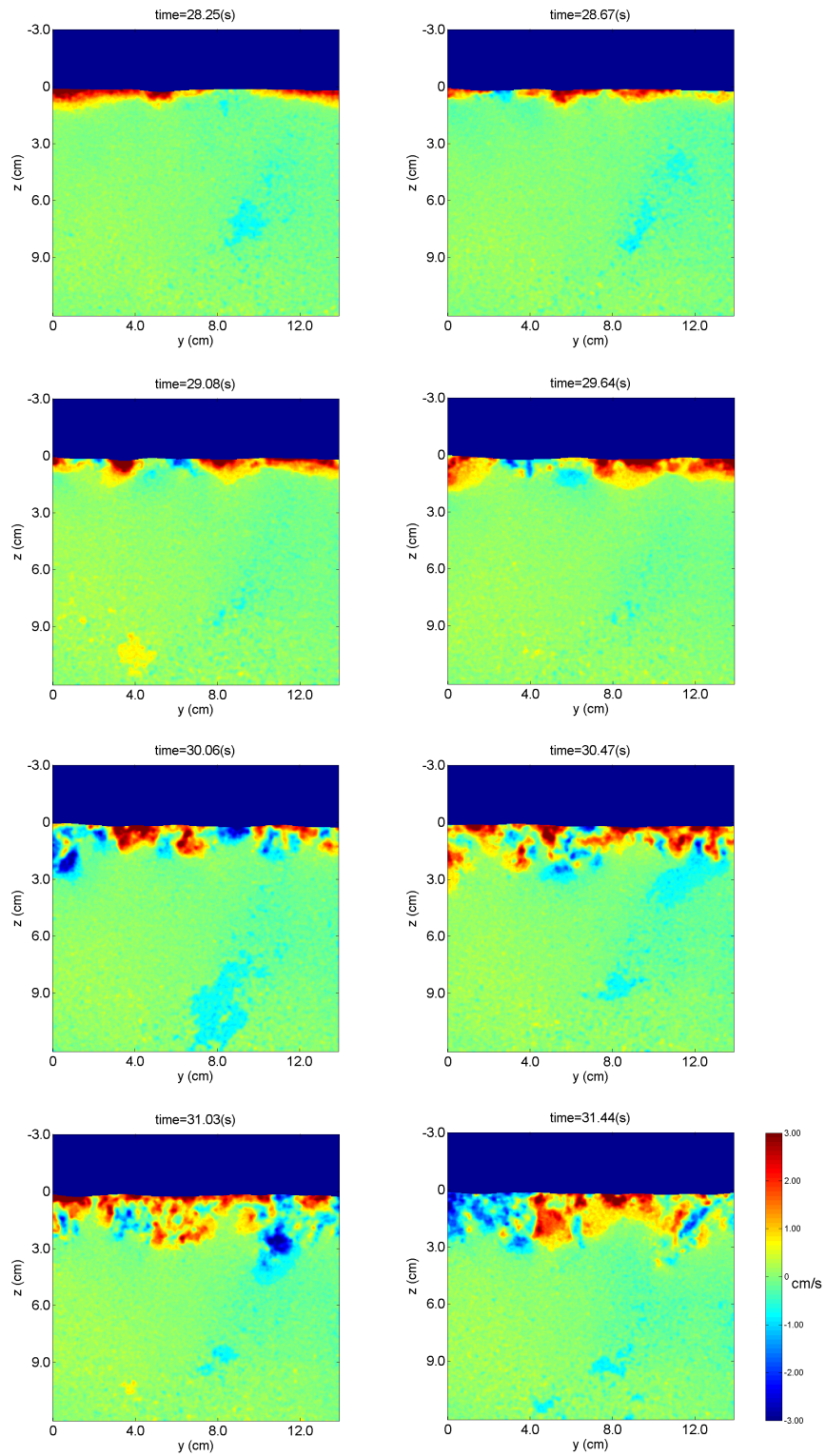


Figure 3.16: The inception and evolution of LC in cross-wind direction of the vertical velocity of Case 1.

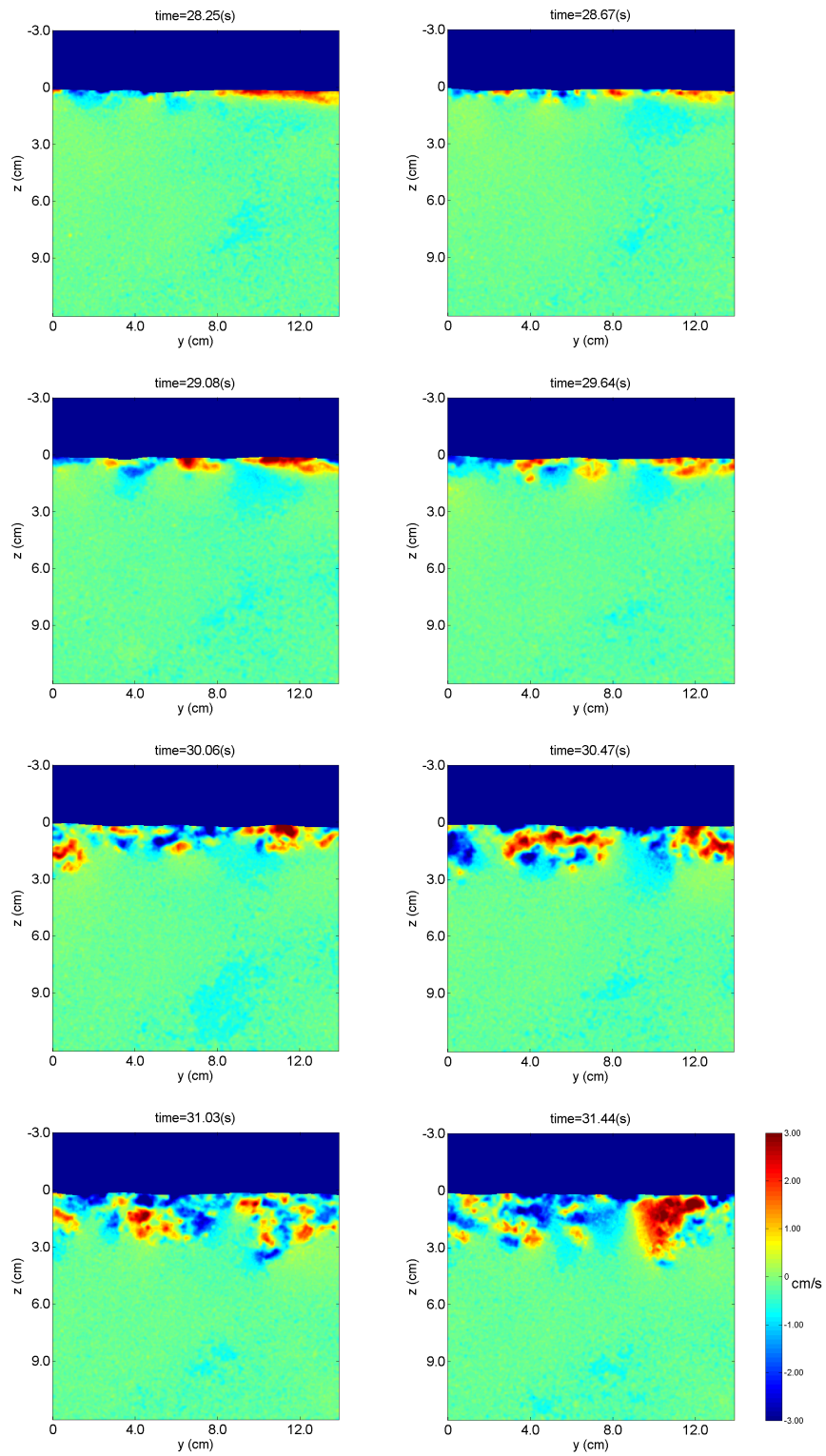


Figure 3.17: The inception and evolution of LC in cross-wind direction of the horizontal velocity of Case 1.

3.4.2 Along-wind direction

In the along-wind direction, the parameters can be measured as the surface was flat. So, we measured the velocity and the vorticity in both the along-wind direction.

3.4.2.1 LC's evolution and horizontal velocity

Figure [3.18](#) is a time series of the horizontal velocity LIF data in the along-wind direction. We can see the fluid movement under water very clearly.

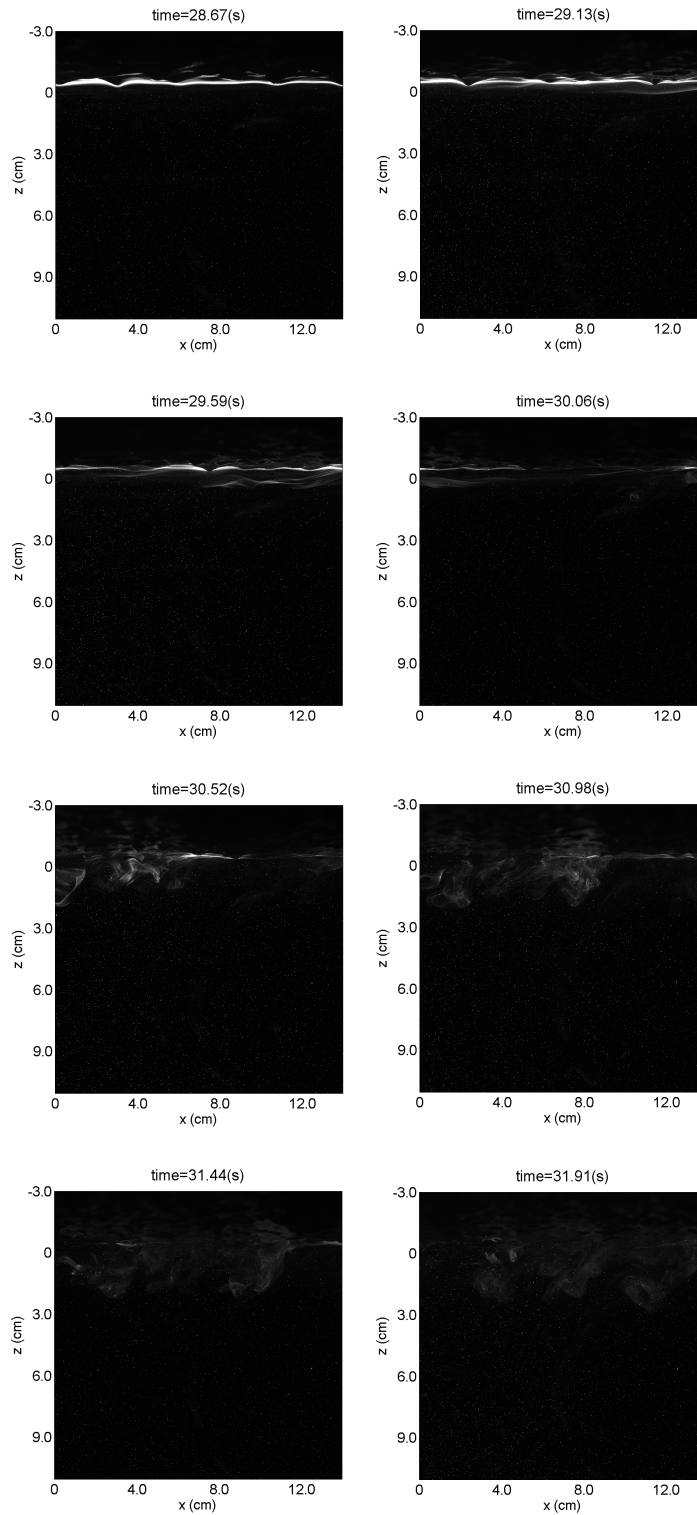


Figure 3.18: The inception and evolution of LC in along-wind direction imaged with LIF of Case 1.

It is concluded that from around 29 s in the Case 1 the LC started to grow and shortly after the flow becomes turbulent. Figure 3.19 further uses the horizontal velocity in along-wind direction to prove it as well.

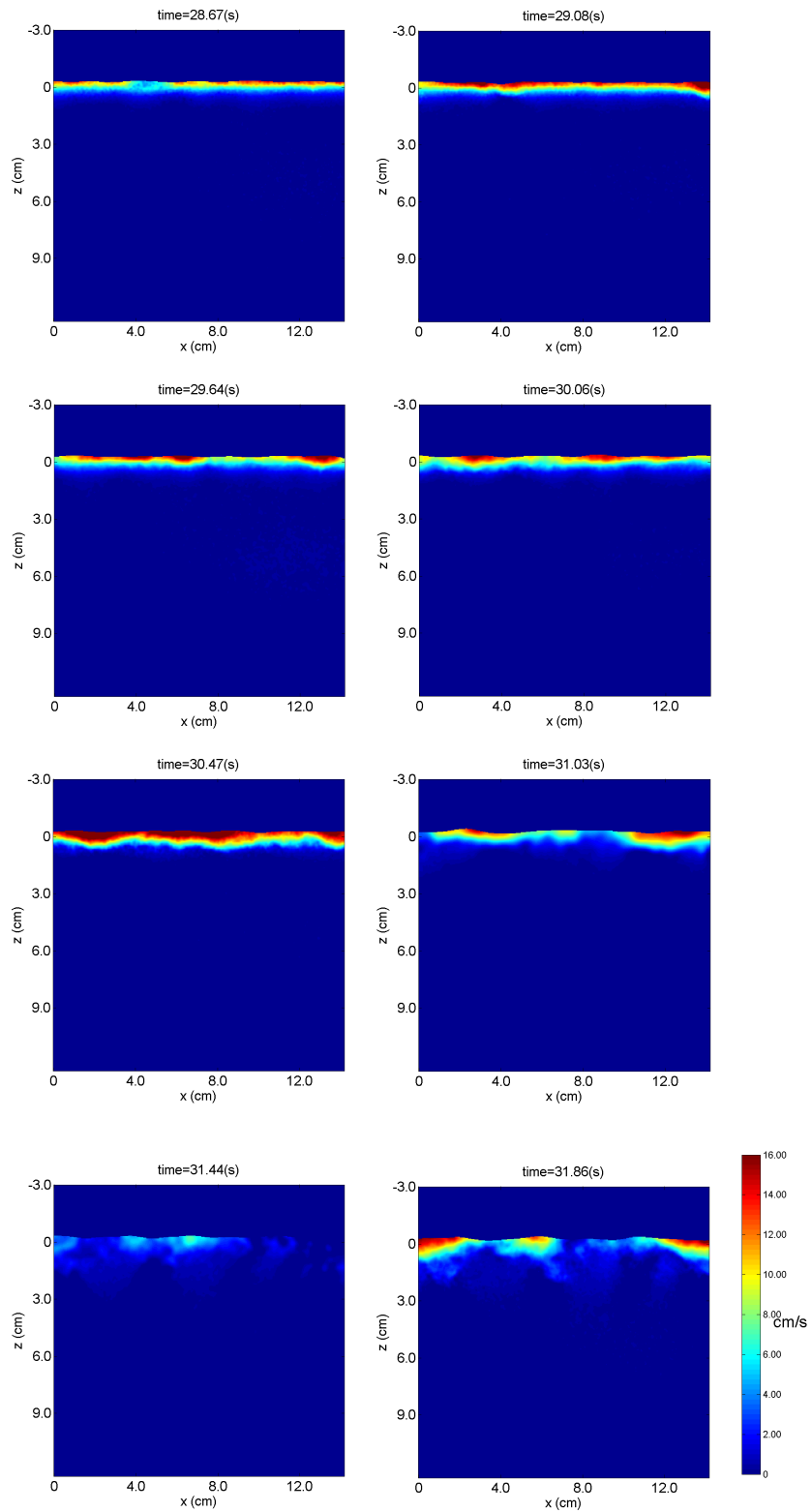


Figure 3.19: The inception and evolution of LC in along-wind direction of the vertical velocity of Case 1. The colorbar indicates the vertical velocity.

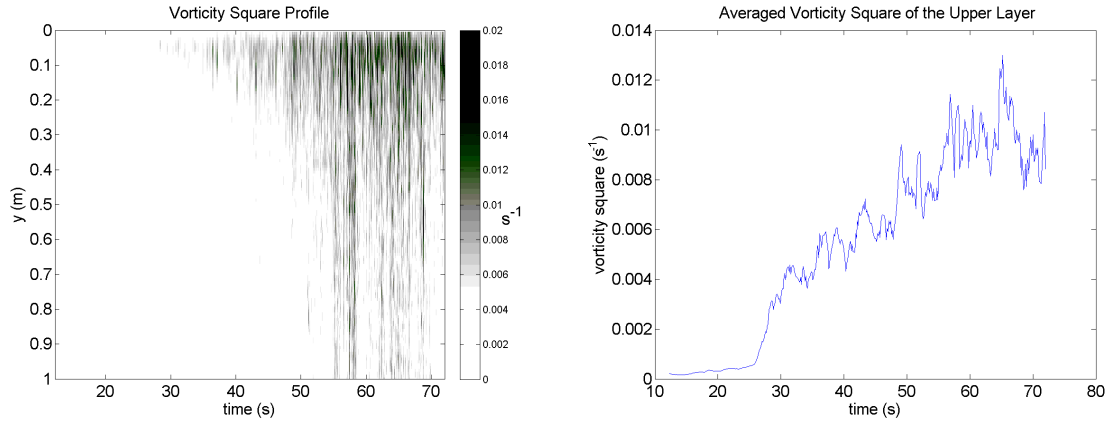


Figure 3.20: The vorticity square profiles and the upper layer of the averaged kinetic energy of Case 1.

The vertical velocity along-wind direction at LC inception time further proves the LC starts from the surface to the depth, as well as the LC helps enhance the mixing.

3.4.2.2 Enstrophy

Besides the velocity, we also measured the vorticity square to indicate the vorticity evolution and development. Figure 3.21 is an example case of the vorticity we measured through PIV data.

Figure 3.20 shows the vorticity square profile and the averaged vorticity square of the upper layer. The left hand side figure are the enstrophy profiles and the right hand side figure shows the time series of the mean enstrophy (integrated in the whole water column) as a function of time.

The enstrophy starts to grow at around 28 s with a sudden increase of the enstrophy indicating the inception of the LC.

Figure 3.21 are the vorticity square profiles and the averaged vorticity square for the upper layers of Case 2, 3, and 4. In all cases, the significant injection of enstrophy in the water column coincides with the inception of the LC.

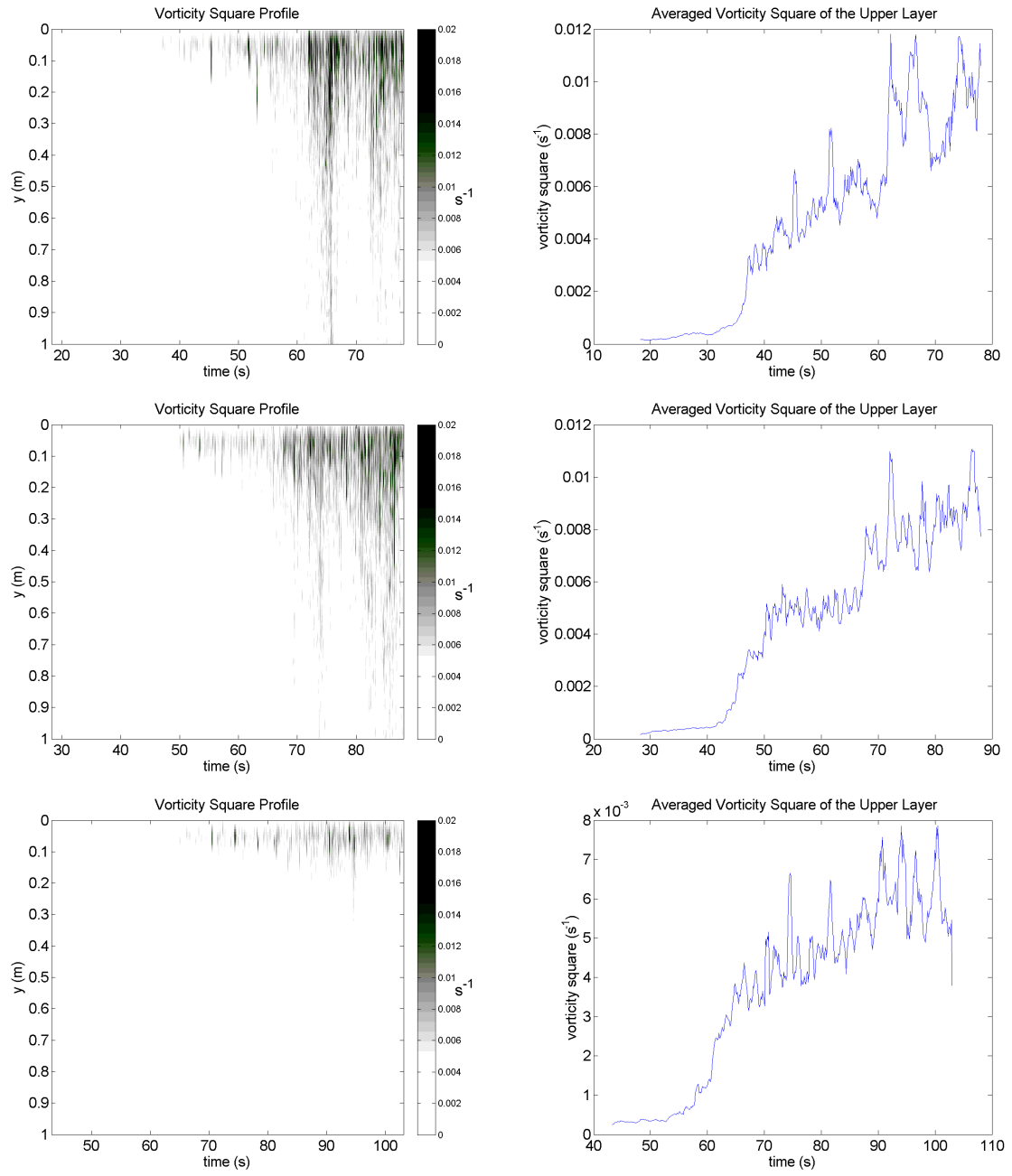


Figure 3.21: The vorticity square profiles and the upper layer of the averaged vorticity square of Case 2, 3, and 4.

3.4.2.3 Velocity

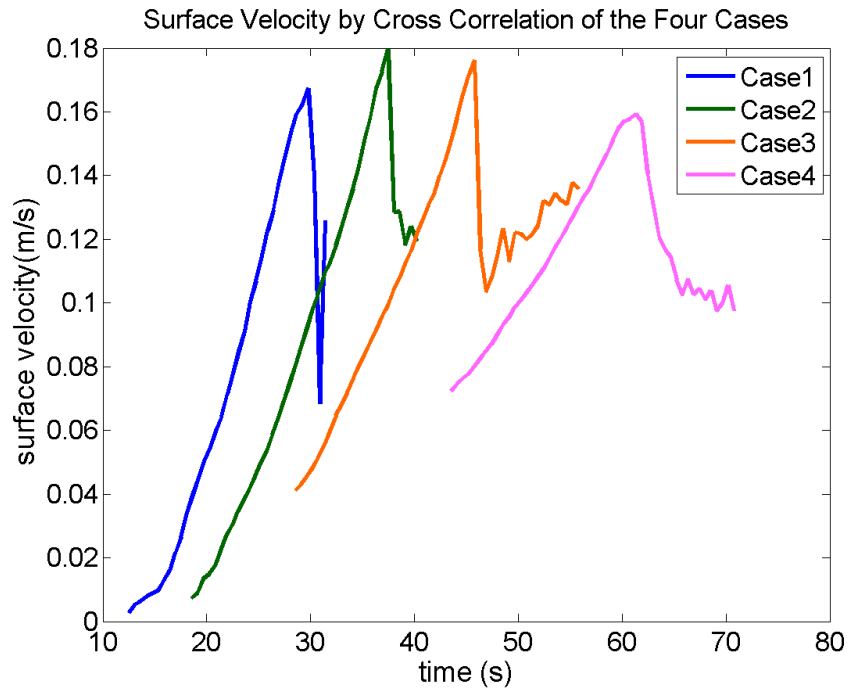


Figure 3.22: Measured surface velocity by cross correlation method of the PIV data along-wind direction.

Figure 3.22 indicates the water velocity by the cross correlation method of the PIV data. The velocity of the Case 1, Case 2, and Case 3 is higher than than the Case 4. Table 3.8 shows the max velocity, time of instability, the velocity acceleration before the LC inception of the surface velocity.

Table 3.7: Summary of surface velocity by cross correlation method of the four cases

Case	Time of instability (s)	Max Velocity (cm/s)	Velocity acceleration before LC (cm/s^2)
1	29.78 ± 0.96	16.92 ± 1.31	1.27
2	37.44 ± 0.32	17.99 ± 0.27	1.10
3	45.78 ± 0.32	17.62 ± 0.49	0.91
4	61.33 ± 0.96	15.93 ± 0.36	0.57

The trend of the water velocity by the cross correlation method matches the trend of the surface velocity by TMV method. By the PIV data, we can estimate the water velocity in along-wind and vertical direction.

Chapter 4

DISCUSSION

4.1 Inception of Surface Waves and Langmuir Circulations

Figure 4.1 shows the comparison of the wind speed, the wave height rms, and the peak frequency of the waves for Case 3. The red dots marked in the figure are the LC inception time. From the figure, it is now evident that the LC appears shortly right after the gravity waves start. Moreover, with the lower wind acceleration, the time period of the beginning of the gravity waves and the LC inception increases.

Figure 4.2 is the peak frequency of the four cases. The red dots here are the LC inception time. From the figure we can see that the LC inception time is always very close to the gravity waves time, however, the larger the wind acceleration is, the closer the time period between the gravity waves inception and LC inception is. It indicates that the instability of the surface shear flow to LC, which is an important transition in the transfer of momentum, heat, and gas across the surface of nature water bodies, and the transfer velocity varies from the wind acceleration.

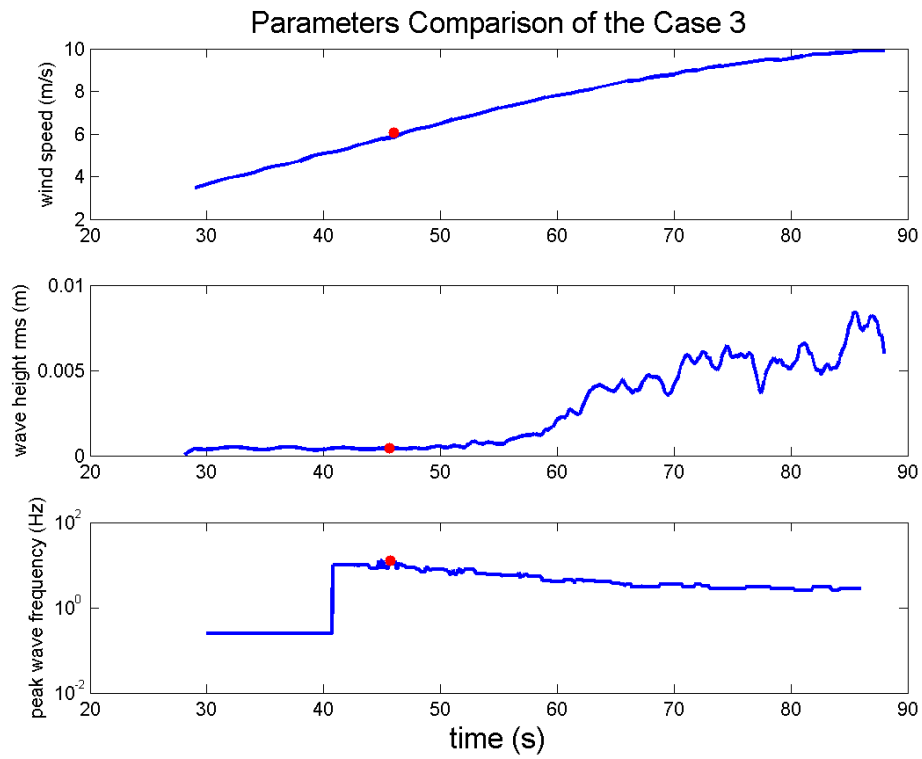


Figure 4.1: Parameters comparison showing the wind speed, the wave height rms, and the wave peak frequency.

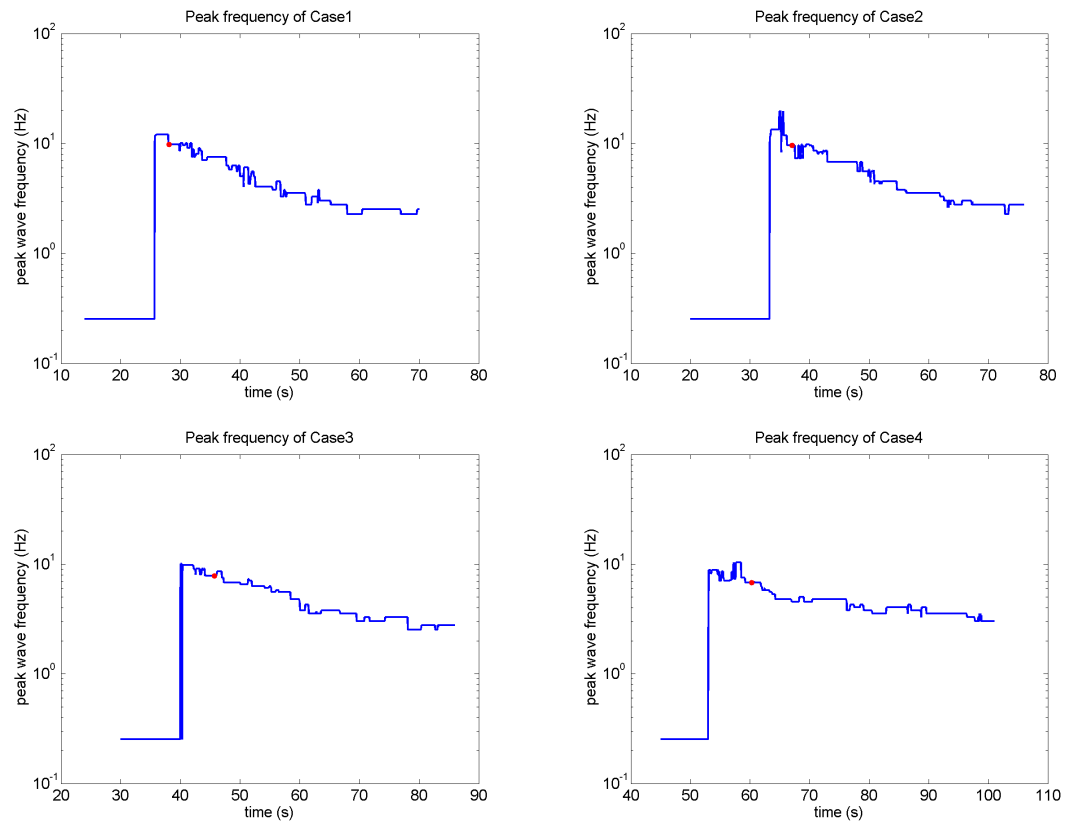


Figure 4.2: Peak frequency for the four cases.

4.2 Comparison between PIV and Infrared Data

4.2.1 Velocity

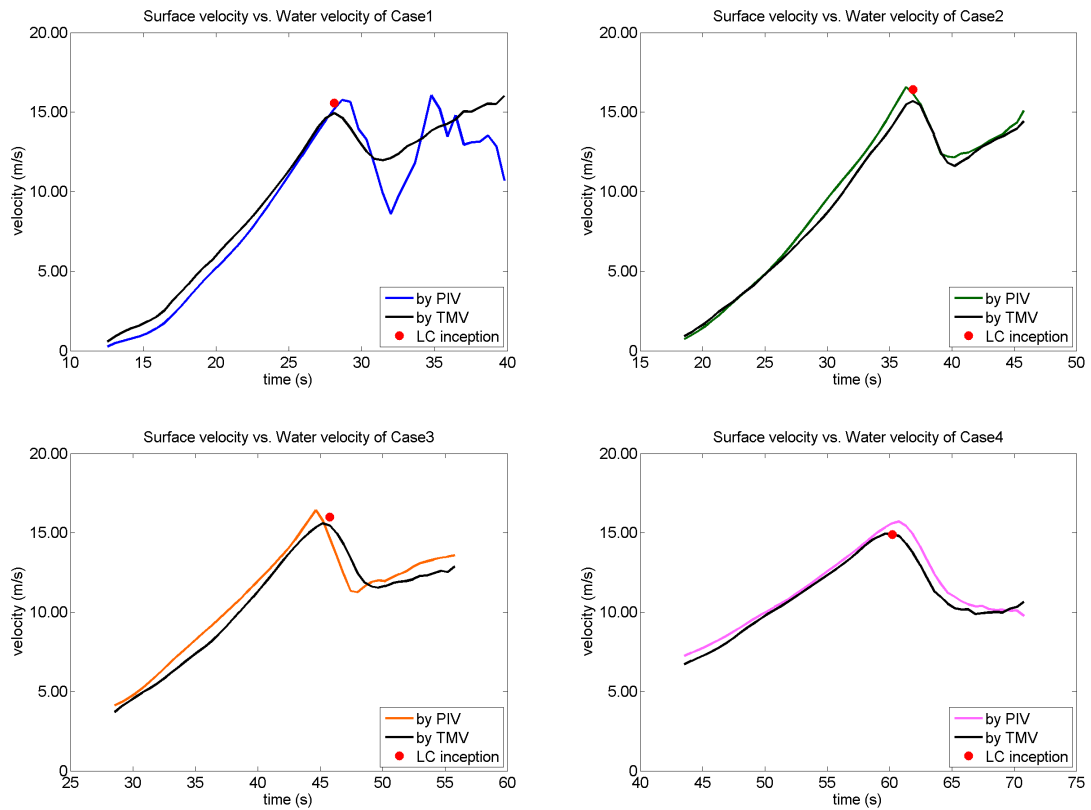


Figure 4.3: Comparison of the velocity by PIV method and TMV method.

Figure 4.3 is the water velocity obtained from the PIV and that obtained from TMV. The red dots in each frame indicates the LC inception time. The velocity calculated by the method of PIV and active infrared imagery are very similar to each other.

Figure 4.4 is the comparison of the velocity obtained from PIV data and infrared data for the four cases. The maximum velocity for the Case 1, 2, and 3 is slightly higher than the maximum velocity of the Case 4.

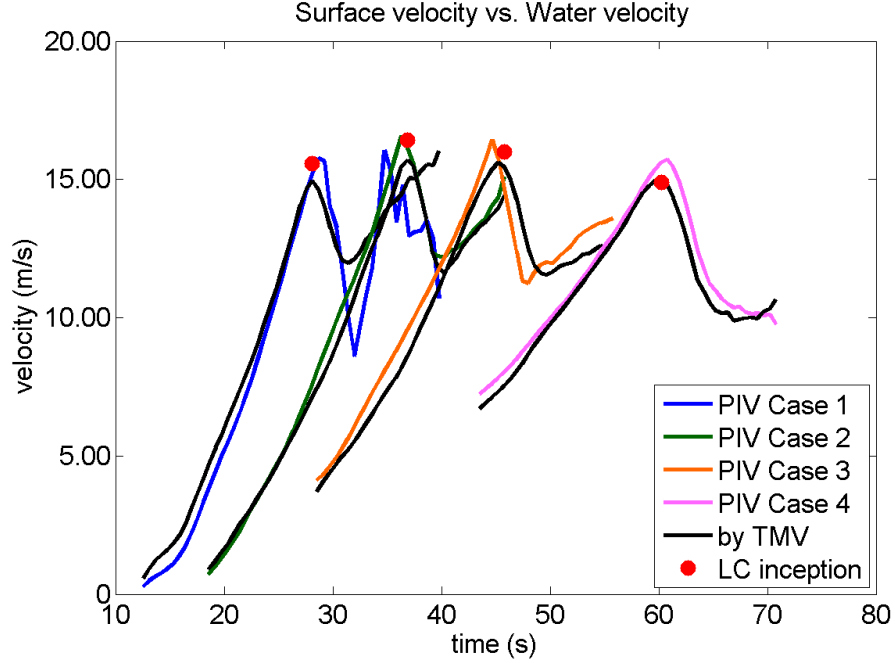


Figure 4.4: Comparison of velocity, vorticity and velocity by PIV method for the four cases.

4.2.2 Other parameters

Figure 4.5 shows the comparison of the surface velocity, vorticity square (enstrophy), decay rate of the active heat markers, and the highpassed temperature standard deviation of the Case 3. From Figure 4.5, we can clearly see that the vorticity square jumps out because of the LC, and the time for the the maximum velocity is the time for the LC inception. For the standard deviation, the time for the maximum standard deviation is the time for the most developed LC evolution time. In this case, Figure 4.5 represents the time relationship of the LC’s inception and evolution as well as its impact on any other parameters like velocity, decay rate of the active heat markers, enstrophy, and temperature standard deviation.

4.3 Comparison of the momentum and heat flux.

Figure 4.6 shows the comparison of the data related to momentum, we put the wind speed, wave height rms, surface velocity and enstrophy in the comparison.

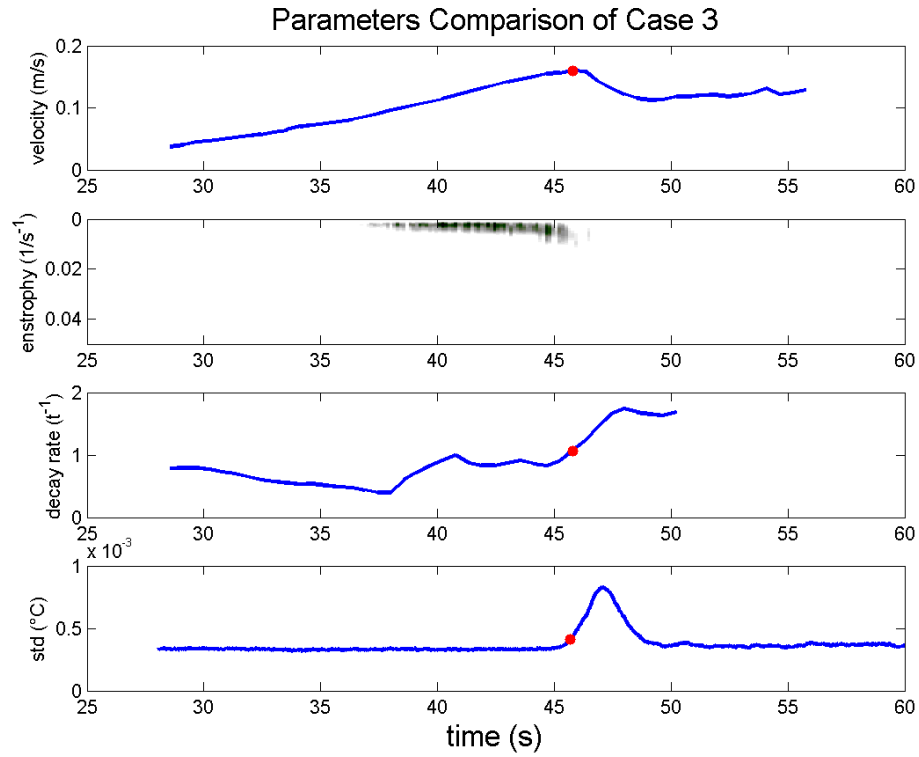


Figure 4.5: Parameters comparison of the surface velocity, vorticity square (entrosphy), surface temperature decay rate, and highpass temperature deviation by the infrared and PIV data and the TMV methods.

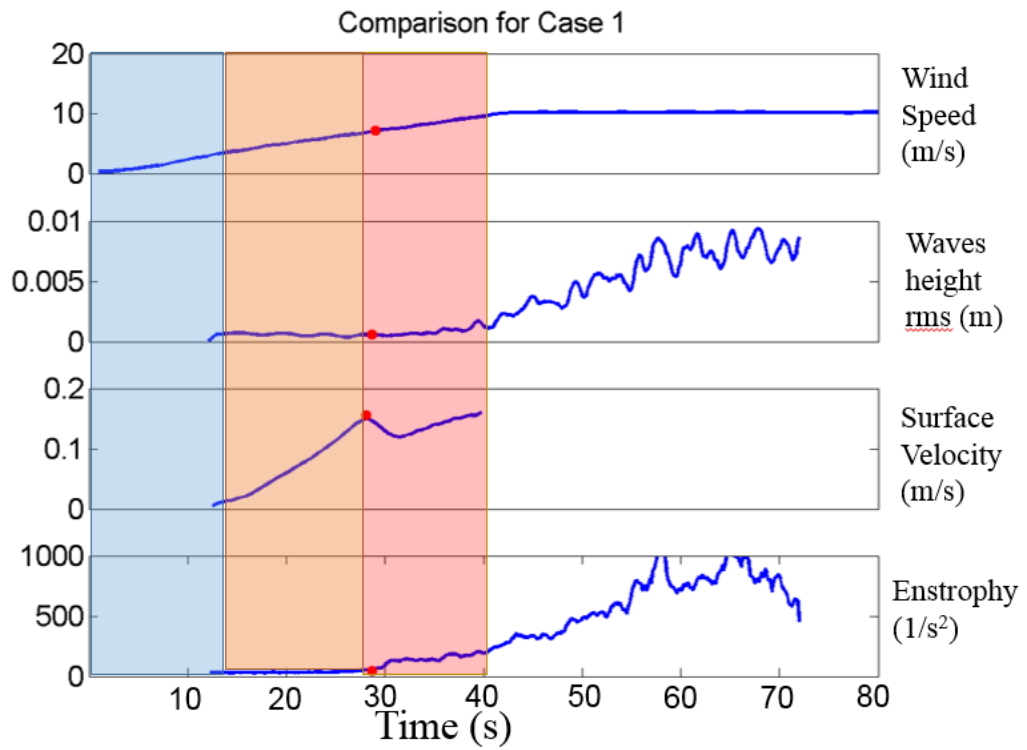


Figure 4.6: The comparison of the momentum data of the Case 1. Different colors means different stage of the flow.

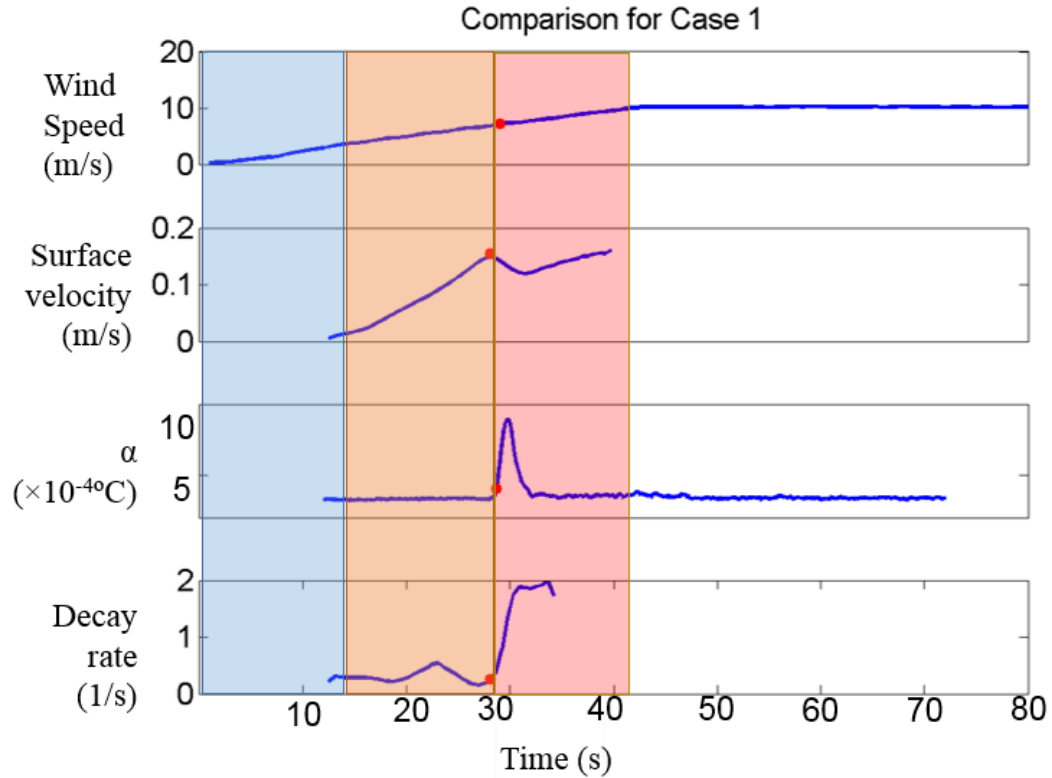


Figure 4.7: The comparison of the thermal data of the Case 1. Different colors means different stage of the flow.

Different colors here indicate different stages of the flow. From Figure 4.6 we can clearly see the four stages of the flow and how the LC represents the transition to the turbulence.

Figure 4.6 shows the comparison of the data related to thermal data, we put the wind speed, surface velocity, highpassed temperature standard deviation and decay rate of the Case 1 in the comparison. Different colors here indicate different stages of the flow. From 4.7 we can clearly see that in spite of the four stages of the flow, the LC transfer the momentum to the depth and help transfer the heat to the air and water.

4.4 Heat and gas flux

From our previous discussion, it is very clear that LC disrupt the momentum boundary layer and enhance the mixing of the surface layer. As a result, LC will also

affect the surface thermal boundary layer.

As in Section 2.2.3, in the Controlled Flux Techniques section, we've already talked about the heat and gas transfer velocity. Meanwhile, the heat and gas fluxes can also be estimated by the heat and gas transfer velocity. In short, the gas flux can be measured by estimating the heat flux.

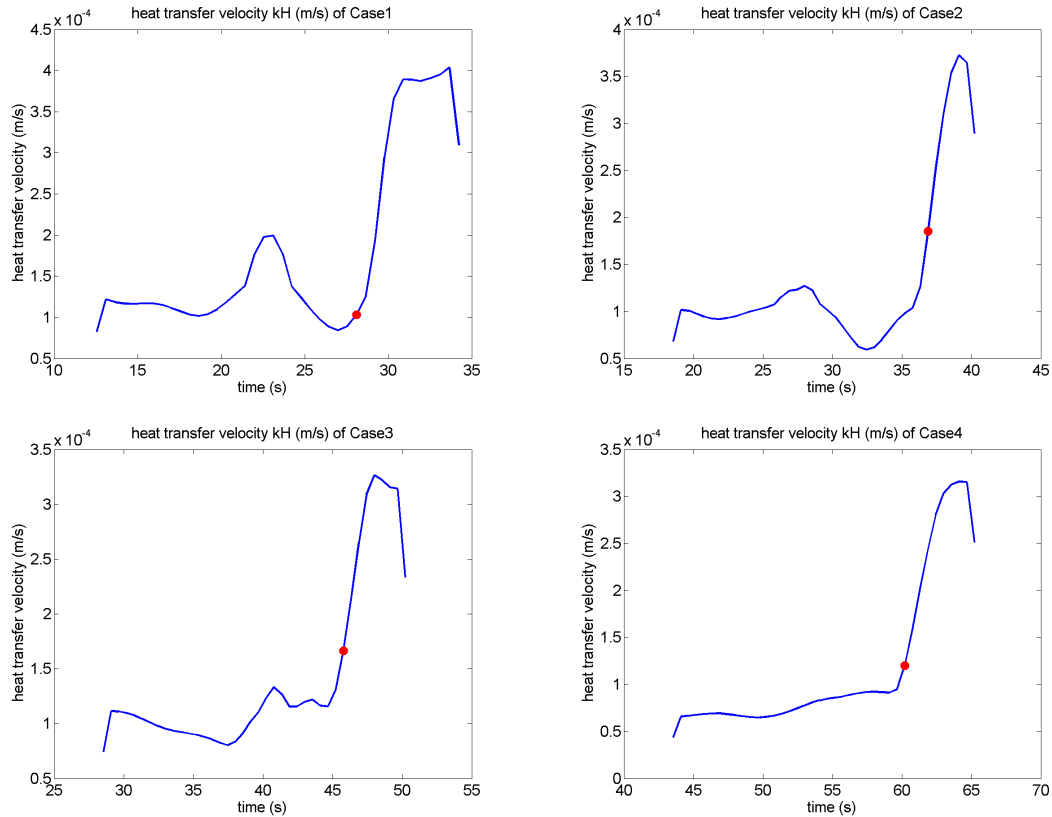


Figure 4.8: The heat transfer velocity of the four cases. The red dots marked in the figure are the LC inception time for each case.

In our research, we set the Schmidt numbers for heat as 7 and the Schmidt numbers for gas as 600. n is a parameter between $1/2$ and $2/3$. However, the trend of the gas transfer velocity keeps the same as the heat transfer velocity.

Figure 4.8 shows the heat transfer velocity of the four cases. From the trend of the heat transfer velocity, it indicates the LC helps and enhances the heat and gas transfer velocities by a factor of 2.8 to 3.8.

In short, for these cases presented here, a 180% increase in heat and gas transfer velocities is measured and can be directly related to the LC inception and the subsequent turbulence. The rapid transition from LC to turbulence plays an important role in the heat and gas transfer in the air-sea interactions.

Table 4.1 summaries the heat and gas transfer velocities, and the heat transfer velocity enhancement as the ratio of the maximum heat transfer velocity to the min heat transfer velocity at the maximum heat transfer velocity time (regarded as the instability time).

4.5 Temperature difference

The mean temperature can be regarded as the skin temperature; and the max temperature can be regarded as the subskin temperature. However, because of instrument noise, fluctuations are present in both these signals. To remedy this, we have taken the difference between skin and subskin temperature, which essentially removes the instrument noise. When the wind is accelerating, the surface temperature monotonically drops due to evaporative cooling. When the LC occur and the flow becomes unstable, ΔT immediately rises up due to the underlying warmer bulk fluid as warm bulk fluid is brought to the surface.

4.6 Scaling the instabilities

4.6.1 Non-dimensional parameters

As in Appendix A, we've talked about the temperature evolution of the water surface. In this case, up to the inception of the LC, the evolution of the surface velocity as well as the surface temperature is monotonic. Therefore, the Reynolds number and Rayleigh number can be estimated from the surface parameter:

$$Re = \frac{U_0 \sqrt{\nu t}}{\nu} \quad (4.1)$$

Table 4.1: Summary of heat and gas flux of the four cases.

Case	Instability Time (s)	Heat transfer velocity ($^{-4}m/s$)	Heat transfer velocity enhancement	Gas transfer velocity ($^{-4}m/s$)
1	30.89	3.179	3.76	29.43-61.80
2	39.11	3.727	3.59	34.51-72.45
3	48.00	3.265	2.82	30.23-63.47
4	64.11	3.157	3.28	29.23-61.37

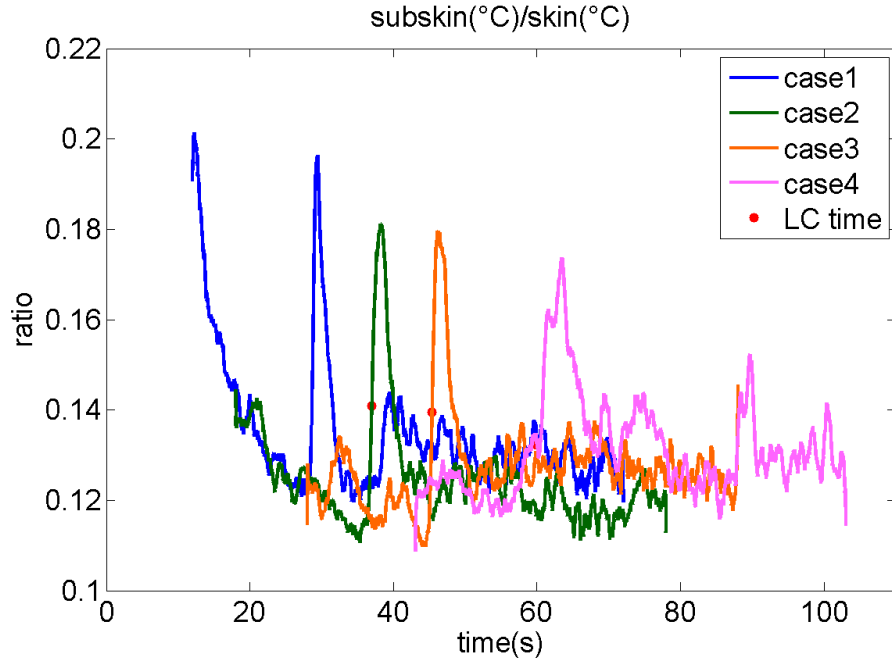


Figure 4.9: The difference, ΔT between maximum temperature and the mean temperature of the four cases. Different color indicates different cases. The red dots are the LC inception time.

Table 4.2: Summary of temperature difference, ΔT between maximum temperature and the mean temperature of the four cases at the LC inception time.

Case	ΔT (C)
1	0.1702
2	0.1650
3	0.1084
4	0.1215

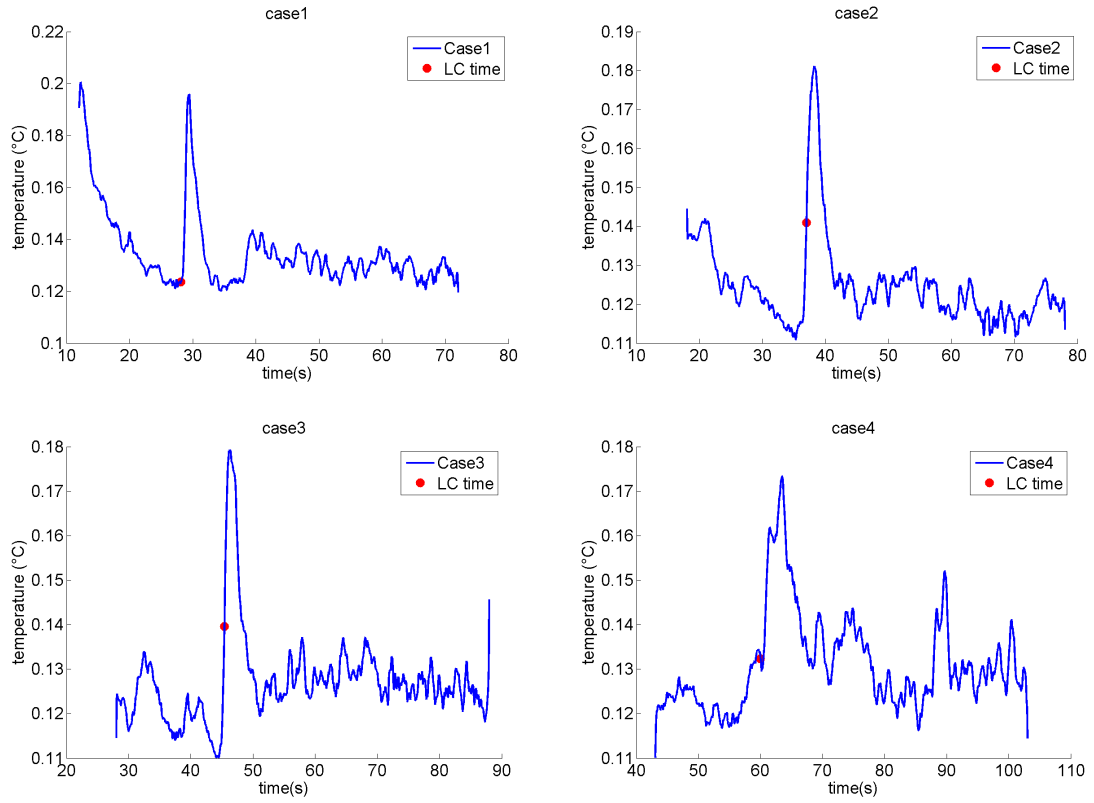


Figure 4.10: The temperature difference, ΔT between maximum temperature and the mean temperature of the four cases. The red dots in the figure are the LC inception time.

Table 4.3: Summary of Reynolds number and Raleigh number of the four cases.

Case	Reynolds number	Raleigh number
1	839	20.57
2	1038	29.31
3	1076	25.56
4	1179	44.03

and

$$Ra = \frac{\alpha(T_0 - T_B)g(\kappa t)^{3/2}}{\kappa\nu} = \frac{\alpha\Delta T_0g(\kappa t)^{3/2}}{\kappa\nu} \quad (4.2)$$

U_0 is the surface water speed, ν is the kinematic viscosity, t is the time after the onset of the wind. α is the thermal expansion coefficient, κ is the thermal diffusivity of the water, and T_B is the bulk temperature.

A direct comparison suggests that the results summarized in 4.3 do not match and compare well with those of Melville et al. (1998) and Veron and Melville (2001). For example, Veron and Melville (2001) stated that the Reynolds number is 530 ± 20 . However, as in Table 4.3, the Reynolds number starts from 840 to 1180, with a comparably larger range than the stable Reynolds number in (Veron and Melville, 2001).

4.6.2 Langmuir number

As stated in Section 1.2, Leibovich (1983) states the dimensionless parameter Langmuir number as

$$La = (v_T^3 k^2 / \sigma a^2 u_*^2)^{1/2} \quad (4.3)$$

Equation 4.1 demonstrates the calculation of Langmuir number, a is the characteristic wave amplitude, σ is the characteristic frequency.

Table 4.4: Summary of Langmuir number and the turbulent Langmuir number for the four cases.

Case	Langmuir number	Inverse Langmuir number	Turbulent Langmuir number
1	0.0032	312.50	0.22
2	0.0058	173.42	0.22
3	0.0062	161.29	0.28
4	0.0061	164.98	0.45

Except for the Langmuir number by [Leibovich \(1977\)](#), [McWilliams et al. \(1997\)](#) also defined a new parameter as “turbulent Langmuir number”

$$La_{turb} = \frac{u_*}{u_s} \quad (4.4)$$

which can also be viewed as ([Thorpe, 2004](#))

$$La_{turb} = (u_*/2S_0)^{1/2} \quad (4.5)$$

u_s is the stokes velocity, u_* is the air friction velocity.

The turbulent Langmuir number usually values about 0.3 in the ocean. It measures the relative influences of directly equilibrium solutions with steady, aligned wind and waves. It can be estimated from observations.

According to $u_s = \sigma ka^2$, and $\sigma = (gk)^{1/2}$, we can retrieve the turbulent Langmuir number as well as the Langmuir number and Inverse Langmuir number in [Table 4.4](#).

BIBLIOGRAPHY

- Asher, W. E., A. T. Jessup, and M. A. Atmane, 2004: Oceanic application of the active controlled flux technique for measuring air-sea transfer velocities of heat and gases. *Journal of Geophysical Research C: Oceans*, **109** (8), 1–13, doi: 10.1029/2003JC001862.
- Craik, A. D. D., 1977: The generation of Langmuir circulations by an instability mechanism. *Journal of Fluid Mechanics*, **81** (02), 209, doi:10.1017/S0022112077001980.
- Doney, S. C., 1995: Irreversible thermodynamics and air-sea exchange. *Journal of Geophysical Research*, **100** (C5), 8541–8553.
- Jain, A. K., 1989: *Fundamentals of Digital Image Processing*, Vol. 14. 569 pp., doi: 10.1002/9780470689776.
- Kenney, B. C., 1993: Observations of coherent bands of algae in a surface shear layer. *Limnology and Oceanography*, **38** (5), 1059–1067.
- Langmuir, I., 1938: Surface Motion of Water Induced By Wind. 119–123 pp., doi: 10.1126/science.87.2250.119.
- Leibovich, B. S., 1977: On the evolution of the system of wind drift currents in the ocean . and Langmuir circulations i Part 1 . Theory and averaged current. **79**.
- Leibovich, S., 1983: The form and dynamics of langmuir circulations. (1868), 391–427.
- McWilliams, J. C., P. P. Sullivan, and C.-H. Moeng, 1997: Langmuir turbulence in the ocean. *Journal of Fluid Mechanics*, **334**, 1–30, doi:10.1017/S0022112096004375.

- Melville, W. K., 1996: The role of surface wave breaking in air-sea interaction. *Annu. Rev. Fluid Mech.*, **28**, 279–321.
- Melville, W. K., R. Shear, and F. Veron, 1998: Laboratory measurements of the generation and evolution of Langmuir circulations. *Journal Of Fluid Mechanics*, **364**, 31–58.
- Pijush K. Kundu, D. R. D. P., Ira M. Cohen, 2012: Chapter 7 Gravity Waves. *Fluid Mechanics*, 253–307, doi:10.1016/B978-0-12-382100-3.10007-1.
- Raffel, M., C. E. Willert, S. Wereley, and J. Kompenhans, 2013: *Particle image velocimetry: a practical guide*. Springer.
- Savelyev, I., E. Maxeiner, and D. Chalikov, 2013: Turbulence Production by Non-breaking Waves.
- Schimpf, U., H. Hauecker, and B. Jhne, 1999: Measurements of Air-Sea Gas Transfer using Active and Passive . . .
- Smith, J. A., 1992: Observed growth of Langmuir circulation. *Journal of Geophysical Research: Oceans*, **97 (C4)**, 5651–5664, doi:10.1029/91JC03118.
- Thorpe, S., 2004: Langmuir Circulation. *Annual Review of Fluid Mechanics*, **36 (1)**, 55–79, doi:10.1146/annurev.fluid.36.052203.071431.
- Veron, F. and W. K. Melville, 2001: Experiments on the stability and transition of wind-driven water surfaces. *Journal Of Fluid Mechanics*, **446**, 25–65, doi:10.1017/S0022112001005638.
- Veron, F., W. K. Melville, and L. Lenain, 2008: Infrared techniques for measuring ocean surface processes. *Journal of Atmospheric and Oceanic Technology*, **25 (2)**, 307–326, doi:10.1175/2007JTECHO524.1.

- Veron, F., W. K. Melville, and L. Lenain, 2011: The Effects of Small-Scale Turbulence on AirSea Heat Flux. *Journal of Physical Oceanography*, **41** (1), 205–220, doi:10.1175/2010JPO4491.1.
- Veron, F., W. K. Melville, F. Veron, and W. K. Melville, 1999: Pulse-to-Pulse Coherent Doppler Measurements of Waves and Turbulence. [http://dx.doi.org/10.1175/1520-0426\(1999\)016<1580:PTPCDM>2.0.CO;2](http://dx.doi.org/10.1175/1520-0426(1999)016<1580:PTPCDM>2.0.CO;2).
- Ward, B., R. Wanninkhof, W. R. McGillis, A. T. Jessup, M. D. DeGrandpre, J. E. Hare, and J. B. Edson, 2004: Biases in the air-sea flux of CO₂ resulting from ocean surface temperature gradients. *Journal of Geophysical Research C: Oceans*, **109** (8), 1–14, doi:10.1029/2003JC001800.
- Weller, R. A., J. P. Dean, J. F. Price, E. A. Francis, J. Marra, and D. C. Boardman, 1985: Three-Dimensional Flow in the Upper Ocean. *Science*, **227** (4694), 401–1556, doi:10.1126/science.227.4694.1552.
- Weller, R. A. and J. F. Price, 1988: Langmuir circulation within the oceanic mixed layer. *Deep Sea Research Part A, Oceanographic Research Papers*, **35** (5), doi:10.1016/0198-0149(88)90027-1.
- Zappa, C., W. E. Asher, and A. T. Jessup, 2001: Microscale wave breaking and air-water the role of microscale area coverage of microscale breaking infrared and wave slope imagery is used to verify that AB detected using IR techniques of Washington. *Journal of Geophysical Research*, **106** (2000), 9385–9391.

Appendix A

TEMPERATURE RATIO

Figure A.1 shows the maximum temperature, the mean temperature, and the ratio of the maximum temperature to the mean temperature for the four cases. It shows how the maximum and mean temperature evolve and develop with the time. We believe this to be due to instrument noise.

Figure A.1 shows the maximum temperature detected in an image (with the marking spots removed). This corresponds to the subskin temperature. We also show the mean image temperature, and the mean-to-max ratio.

The ratio shows a bit of a decrease before the LC as the wind picks up and cools the thermal molecular layer. The inception of the LC mixes subskin fluid to the surface and corresponds to a sudden increase in the temperature ratio. Once the flow is turbulence, that ratio (i.e. the ratio between surface and subskin temperature) becomes constant. The trend of the ratio indicates that the heat transfer velocity and the heat flux were enhanced by the LC.

In Figure A.2, we uses different color lines to put the time series of the ratio of the four cases together, it shows whole 60 seconds for each case. The red dots in figure A.2 are the LC inception time. Almost the same trend as the temperature standard deviation, the ratio of Case 4 is smaller than the first three cases and the time length scale between the time of LC inception and the time when the flow becomes fully turbulent is much longer.

In Table A.1, we measured and compared the ratio of the maximum to the mean temperature before the LC inception and after LC inception. The ratio of the maximum temperature to the mean temperature before LC inception are almost the

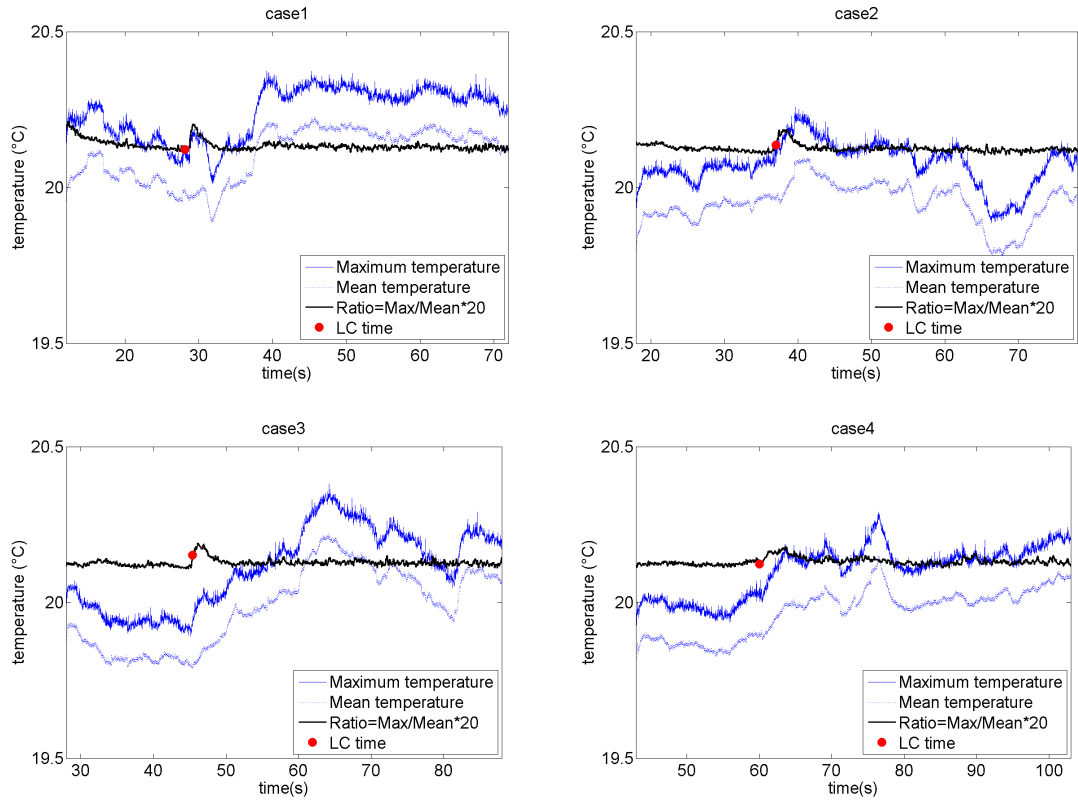


Figure A.1: The maximum temperature, the mean temperature, and the ratio of maximum temperature to the mean temperature of four cases. The red dots in the figure are the LC inception time.

Table A.1: Summary of ratio of the maximum temperature to mean temperature of the infrared temperature data.

Case	Max Ratio (s)	Mean ratio before LC (m/s ²)	Mean ratio after LC (m/s ²)	Ratio of max to mean ratio before LC	Ratio of max to mean ratio after LC	Time period (s)	Time length (s)
1	1.0063	1.0131	1.0082	1.0068	1.0048	28.38-33.12	4.74
2	1.0062	1.0115	1.0066	1.0052	1.0049	36.96-41.83	4.87
3	1.0063	1.0119	1.0065	1.0056	1.0053	45.10-51.33	6.23
4	1.0065	1.0109	1.0061	1.0044	1.0047	59.92-67.41	7.47

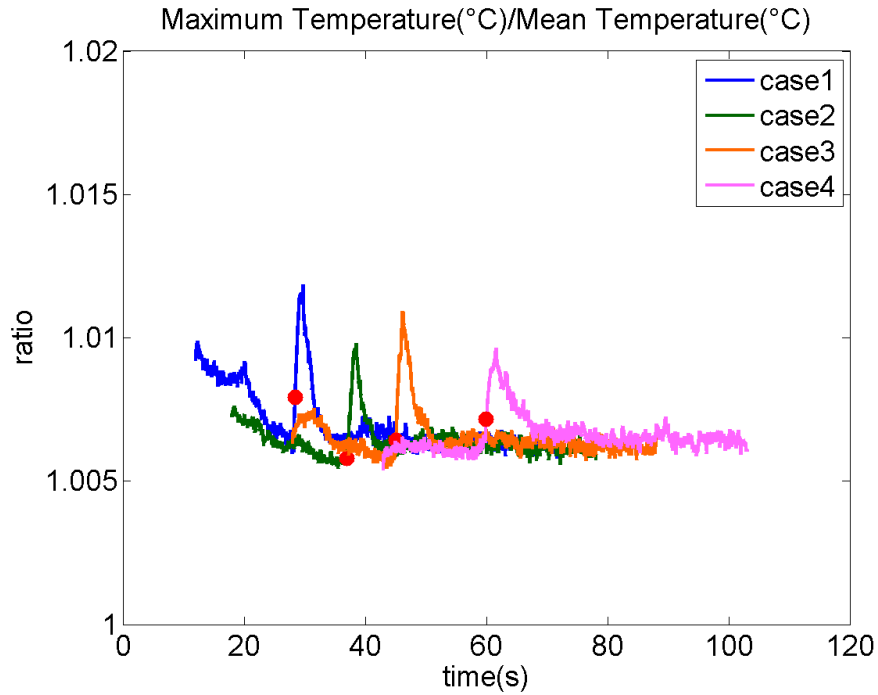


Figure A.2: The ratio of maximum temperature to the mean temperature of the four cases. Different color indicates different cases. The red dots are the LC inception time.

same value and magnitude of the ratio of the maximum temperature to the mean temperature after LC, while only at the LC inception time, the ratio of the maximum temperature to the mean temperature rises to the higher value, which further proves our assumption: the LC helps mix the thermal boundary layer and enhance the heat flux.